Dynamic accuracy analysis of a 5PSS/UPU parallel mechanism based on rigid-flexible coupled modeling

Yanbiao Li
Zhejiang University of Technology
Zesheng Wang
Zhejiang University of Technology
Chaoqun Chen
Zhejiang University of Technology
Taotao Xu
Zhejiang University of Technology
Bo Chen (chenb@zjut.edu.cn)
Zhejiang University of Technology

Original Article

Keywords: parallel mechanism, geometric error, calibration algorithm, elastodynamic model, dynamic accuracy

Posted Date: December 22nd, 2020

DOI: https://doi.org/10.21203/rs.3.rs-132642/v1

Dynamic accuracy analysis of a 5PSS/UPU parallel mechanism based on rigid-flexible coupled modeling

Yanbiao Li[1,2], Zesheng Wang[1,2], Chaoqun Chen[1,2], Taotao Xu[1,2], Bo Chen[1,2,*]

Abstract

In order to improve the low output accuracy caused by the elastic deformations of the branch chains, a finite element-based dynamic accuracy analysis method for parallel mechanisms is proposed in this paper. First, taking a 5–prismatic–spherical–spherical (PSS)/universal–prismatic–universal (UPU) parallel mechanism as an example, the error model is established by a closed vector chain method while its influence on the dynamic accuracy of the parallel mechanism is analyzed through numerical calculation and simulation. According to the structural and error characteristics of the parallel mechanism, a vector calibration algorithm is proposed to reduce the position and pose errors along the whole motion trajectory. Then, considering the elastic deformation of the rod, the rigid-flexible coupling dynamic equations of the mechanism are established by combining the finite element method with the Lagrange method, and the equations are vectorially superimposed by means of internal force cancellation to synthesize the elastic dynamics equation of the connecting rod. Based on the constraint condition of each moving part, the elastodynamic model of the whole machine is obtained. Furthermore, the effect of component flexibility on the dimensionless root mean square error of the displacement, velocity and acceleration of the moving platform is investigated by using a Newmark method, and the dynamic accuracy influenced by these dimensionless root mean square errors is further studied. The research work establishes an important theoretical foundation for the development of the prototype.

Keywords: parallel mechanism, geometric error, calibration algorithm, elastodynamic model, dynamic accuracy

1 Introduction

Compared with the serial mechanism, the parallel mechanism has advantages of greater stiffness, higher precision, reduced inertia, and higher payload to weight ratio [1-4]. It has been widely used in aerospace, food processing, vehicle and ship industry, and medical equipment fields [5-8].

The process of mechanical part processing and assembly will produce inevitable geometric errors, which will lead to unfavorable impacts on the accuracy of the parallel mechanism. The error calibration method can effectively reduce the influence of geometric errors on the accuracy of the parallel mechanism [9, 10]. The quality of calibration methods directly determines the effect of error calibration. Commonly geometric error calibration methods include external calibration, constraint calibration and self-calibration. The external calibration method [11-13] directly measures the pose of the mechanism through external precision measuring equipment, and then identifies the geometric parameters of the moving platform. However, it has several disadvantages such as low calibration efficiency, high cost, and poor external anti-interference ability, etc. The constraint calibration method [14-16] restricts the partial movement ability of the mechanism components by imposing constraints on the system, and then kinematic calibration can be performed. Compared with the external calibration method, the constraint calibration method is relatively simple to operate and does not require expensive external measuring equipment, but it restricts the mechanical part motion characteristics, which makes it difficult to identify all kinematic parameters. The self-calibration method [11, 14, 17] of measuring equipment is used by the extra redundant information of the moving platform to identify its geometric parameters. However, the design of a measurement method for redundant information is needed, and all geometric parameters are hard to be identified. Meanwhile, the error calibration can improve the motion accuracy of the mechanism, which is of great significance to the dynamic accuracy analysis of the parallel mechanism [18, 19].

Dynamic accuracy is an important performance evaluation index for a parallel mechanism [20-22], which requires the actual motion state of the mechanism to be identical with the desired motion state. Accordingly, the designer needs to study the influence law of error factors on the dynamic accuracy of the parallel mechanism in the design stage of the mechanism. The performance of the

*Correspondence: chenb@zjut.edu.cn
[1] Key Laboratory of E & M, Ministry of Education & Zhejiang Province, Zhejiang University of Technology, Hangzhou 310032, China
Full list of author information is available at the end of the article.

system is often significantly reduced while the failure rate will increase or even cause major losses if these error factors are not fully taken into account. Therefore, the dynamic accuracy of a precision mechanism is worthy of in-depth study. Yun and Li [23] adopted a kind of wide-range flexure hinge and established a kinematics model of an 8-PSS/SPS parallel mechanism system via the stiffness model and Newton–Raphson method. Kane's method was used to build up the dynamics model for analyzing the workspace, motion precision and dynamic characteristics. Bhutani and Dwarakanath [24] obtained the synthesis of leg ranges of a 3-DOF UPU parallel mechanism from sensitivity analysis. Based on the design and sensitivity analysis, the parallel mechanism was developed and various experiments have shown that the manipulator exhibited high accuracy and precision. Alberto [25] derived its elastic dynamic equations by using a flat-shaped parallel robot, and the effects of two commonly used static balancing techniques on the dynamic performance of closed-chain mechanisms were deeply studied. Pira [26] tooka plane high-precision linkage as the object, the finite element method was used to derive its elastodynamic equation, and its dynamic characteristics and natural frequency were analyzed. Taking the plane 3-PRR parallel mechanism as the object, ZHANG [27] established a mechanism dynamics model with the clearance of the rotating pair, and proposed an RMSE index to quantify the effect of joint clearance on the dynamics of the system. As discussed above, the rigid body models were usually adopted as the research object, and the finite element method was used for analyzing the dynamic accuracy of the planar parallel mechanism. There are few related studies on dynamic accuracy caused by the elastic deformation of the spatial parallel mechanism.

The dynamic equation of the parallel mechanism is extremely complicated with the flexible deformation taken into account. However, the elastic deformation of the branch chain of the mechanism will cause elastic vibration, which leads to the pose error of the moving platform [28, 29]. Therefore, the study of flexible deformation is very important to improve the dynamic accuracy of the mechanism. Taking a 5PSS/UPU coupling mechanism as an example [30, 31], a closed vector chain method is proposed to reduce the influence of geometric errors on dynamic accuracy. Combing the finite element method with Lagrange method, the rigid-flexible coupling elastic dynamic equation of the system was established, and the effect of dynamic accuracy of component flexibility on the parallel mechanism was further analyzed. Finally, the design principle for the mechanism parameter of the prototype was obtained.

This paper is organized as follows. Section 2 studies the influence of geometric error on the dynamic accuracy of the 5-PSS/UPU parallel mechanism and the calibration of geometric errors for the parallel mechanism. Section 3 establishes the elastodynamic model and analyzes the influence of the flexibility of the links on the dynamic accuracy of the parallel mechanism. Subsequently, numerical simulations are carried out. Section 4 outlines the conclusions.

2 Analysis of the influence of geometric error on dynamic accuracy

2.1 Error modeling of 5-PSS/UPS parallel mechanism

The basic structure of the 5-PSS/UPU parallel mechanism is shown in Fig. 1. It consists of a fixed base and a moving platform connected using six branch chains. The six branches include five PSS joint branches and one UPU joint branch. The PSS joint branch chains are symmetrical and the power input of the parallel mechanism system, and the UPU joint branch chain only provides constraints to institutions. Each drive branch is composed of 1 moving pair and 2 spherical pairs. The moving pair is the driving pair of the mechanism driven by the linear motor module. The structure diagram of the 5-PSS/UPU parallel mechanism is shown in Fig. 2, which depicts the fixed coordinate system *O-XYZ* and moving coordinate system $D\text{-}X_DY_DZ_D$. *D* and *O* are the centers of the moving and fixed platforms respectively. The *Z* axis is perpendicular to the static platform, the *X* axis is from the coordinate origin to point A_1, and the *Y* axis is determined by the right-hand rule. *T*he Z_D axis is perpendicular to the moving platform upwards, the X_D axis is from the coordinate origin to point C_1, and the Y_D axis is determined by the right-hand rule. $E_i\text{-}X_{Ei}Y_{Ei}Z_{Ei}$ is the local coordinate system where the origin coincides with A_i, the Y_{Ei} axis coincides with A_iB_i, the X_{Ei} axis is perpendicular to OE_i, and the z-axis is determined by the right-hand rule, where i=1,2,3,4,5,6.

In the fixed coordinate system *O-XYZ*, the error model of the 5-PSS/UPU mechanism is established by vector method. The vector closed loop equation of a branch of the parallel mechanism can be expressed as

$$\boldsymbol{D} + {}^{O}_{D}\boldsymbol{R}\,{}^{D}\boldsymbol{C}_i = \boldsymbol{A}_i + l_i\boldsymbol{s}_i + L_i\boldsymbol{n}_i \tag{1}$$

where $\boldsymbol{D}$ and ${}^{O}_{D}\boldsymbol{R}$ are the position vector and rotation matrix of the coordinate origin of the dynamic coordinate system $D\text{-}X_DY_DZ_D$ in the fixed coordinate system *O-XYZ*, $\boldsymbol{s}_i$ denotes the direction vector of the i-th driving branch. $\boldsymbol{n}_i$ represents the direction vector of the link of the i-th branch.

Assuming that all error sources are small variables, differentiating Eq. (1) can be rewritten as

$$\begin{aligned} &\boldsymbol{d}_D + \mathrm{d}\,{}^{O}_{D}\boldsymbol{R}\cdot{}^{D}\boldsymbol{C}_i + {}^{O}_{D}\boldsymbol{R}\cdot\mathrm{d}\,{}^{D}\boldsymbol{C}_i \\ &= \mathrm{d}\boldsymbol{A}_i + \mathrm{d}l_i\boldsymbol{s}_i + l_i\mathrm{d}\boldsymbol{s}_i + \mathrm{d}L_i\boldsymbol{n}_i + L_i\mathrm{d}\boldsymbol{n}_i \end{aligned} \tag{2}$$

where $\boldsymbol{d}_D = [\mathrm{d}x_D, \mathrm{d}y_D, \mathrm{d}z_D]^{\mathrm{T}}$, $\mathrm{d}\,{}^{O}_{D}\boldsymbol{R} = \boldsymbol{\varepsilon}_D \times {}^{O}_{D}\boldsymbol{R}$.

$\boldsymbol{\varepsilon}_D = [\mathrm{d}\gamma_D, \mathrm{d}\beta_D, \mathrm{d}\alpha_D]^{\mathrm{T}}$ represents the differentiation of the rotation angle of the moving platform around the *X*, *Y* sand *Z* axes.

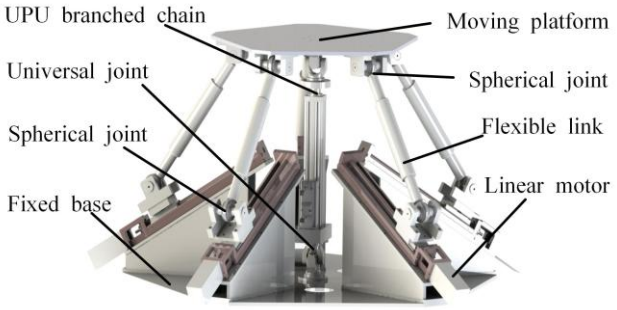

Figure 1 Virtual prototype of 5-PSS/UPU parallel mechanism

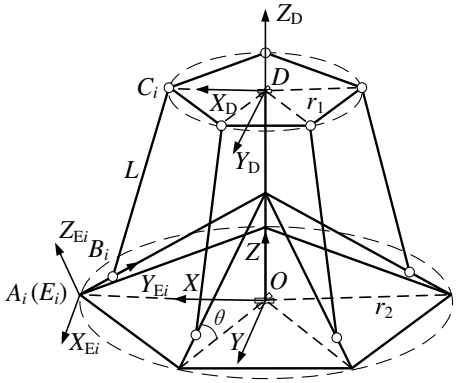

Figure 2 Structure diagram of 5-PSS/UPU parallel mechanism

Equation (2) can be rewritten by taking the dot products of both sides with vector $\boldsymbol{n}_i^{\mathrm{T}}$ as

$$\begin{aligned}&\boldsymbol{n}_i^{\mathrm{T}}\boldsymbol{d}_D + \boldsymbol{n}_i^{\mathrm{T}}\boldsymbol{\varepsilon}_D \times \boldsymbol{r}_{DCi} + \boldsymbol{n}_i^{\mathrm{T}}\,{}_D^O\boldsymbol{R}\cdot \mathrm{d}\,{}^D\boldsymbol{C}_i \\ &= \boldsymbol{n}_i^{\mathrm{T}}\mathrm{d}\boldsymbol{A}_i + \boldsymbol{n}_i^{\mathrm{T}}\mathrm{d}l_i\boldsymbol{s}_i + \boldsymbol{n}_i^{\mathrm{T}}l_i\mathrm{d}\boldsymbol{s}_i + \boldsymbol{n}_i^{\mathrm{T}}\mathrm{d}L_i\boldsymbol{n}_i + \boldsymbol{n}_i^{\mathrm{T}}L_i\mathrm{d}\boldsymbol{n}_i\end{aligned} \tag{3}$$

Since the error is a small variable, it can be approximated as a kind of differentiation. The error mapping model of the parallel mechanism can be expressed as

$$\boldsymbol{J}_W\delta\boldsymbol{W} = \delta\boldsymbol{\Lambda} + \boldsymbol{G}_L\delta\boldsymbol{L} + \boldsymbol{G}_C\delta\,{}^D\boldsymbol{C} + \boldsymbol{G}_A\delta\boldsymbol{A} + \boldsymbol{G}_S\delta\boldsymbol{S} \tag{4}$$

where $\delta\boldsymbol{W}$ denotes the position and pose error of the moving platform. $\delta\boldsymbol{\Lambda}$ represents the input error of driving displacement. $\delta\boldsymbol{L}$ is the length error of a fixed link. $\delta\,{}^D\boldsymbol{C}$ is the position error of the spherical hinge at the moving platform. $\delta\boldsymbol{A}$ is the error of the apical position of the linear actuator. $\delta\boldsymbol{S}$ is the direction error of the linear actuator. $\boldsymbol{J}_W$ is the Jacobian matrix of error transmission. $\boldsymbol{G}_L$ is the coefficient matrix of link length error. $\boldsymbol{G}_C$ is the coefficient matrix of the position error of spherical hinge at the moving platform. $\boldsymbol{G}_A$ is the coefficient matrix of apical position error of linear actuator. $\boldsymbol{G}_S$ is the error coefficient matrix of the linear actuator direction.

When the parallel mechanism is in a nonsingular configuration, the Jacobian matrix of error transmission is invertible. Eq. (4) can be abbreviated as

$$\delta\boldsymbol{W} = \boldsymbol{K}\delta\boldsymbol{p} \tag{5}$$

with $\begin{cases}\boldsymbol{K} = \boldsymbol{J}_W^{-1}[\boldsymbol{E}_5\ \boldsymbol{G}_L\ \boldsymbol{G}_C\ \boldsymbol{G}_A\ \boldsymbol{G}_5] \\ \delta p = [\delta\boldsymbol{\Lambda}^{\mathrm{T}}\ \delta\boldsymbol{L}^{\mathrm{T}}\ \delta\boldsymbol{C}^{\mathrm{T}}\ \delta\boldsymbol{A}^{\mathrm{T}}\ \delta\boldsymbol{S}^{\mathrm{T}}]\end{cases}$.

where $\boldsymbol{K}$ represents the mapping matrix of geometric error. $\delta\boldsymbol{p}$ denotes the geometric error source of the parallel mechanism, $\delta\,{}^D\boldsymbol{C}$, $\delta\boldsymbol{A}$ and $\delta\boldsymbol{S}$ all have errors in the *x*, *y* and *z*-axis directions.

There are 11 error sources of the parallel mechanism in $\delta\boldsymbol{p}$ of Eq. (5). Among them, the *z*-direction error of linear actuator apex δA_z is 0. Since the direction vector of linear actuator along the *x*, *y* and *z* axes of the three errors are not independent of each other, two independent error parameters (declinations $\delta\varphi$ and $\delta\theta$) are used to facilitate the analysis of error sensitivity, as shown in Fig. 3.

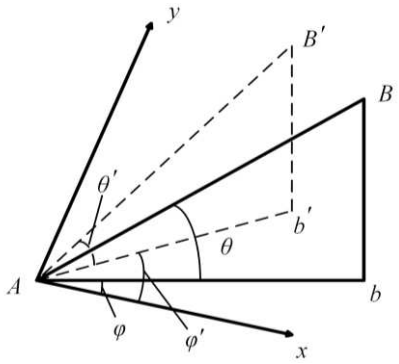

Figure 3 Linear motor direction vector error angle

where $\delta\varphi = \varphi' - \varphi$, $\delta\theta = \theta' - \theta$. The relationship between $\delta\varphi$, $\delta\theta$ and δs_x, δs_y, δs_z can be expressed as

$$\begin{cases}\delta s_x = \cos(\delta\theta + \theta)\cos(\delta\varphi + \varphi) - \cos(\theta)\cos(\varphi) \\ \delta s_y = \cos(\delta\theta + \theta)\sin(\delta\varphi + \varphi) - \cos(\theta)\sin(\varphi) \\ \delta s_z = \sin(\delta\theta + \theta) - \sin(\theta)\cos(\varphi)\end{cases} \tag{6}$$

Both φ and θ are known quantity. The expressions of $\delta\varphi$ and $\delta\theta$ can be derived from Eq. (6), so 11 error sources can be reduced to 9 independent error sources.

2.2 Influence of geometric error on dynamic accuracy

In terms of Eq. (6), the geometric error mapping matrix $\boldsymbol{K}$ is closely related to the moving platform's position and pose. Therefore, the analysis of the geometric error is very important to the dynamic accuracy of the parallel mechanism. The analysis process of the influence of geometric errors on dynamic accuracy is shown in Fig. 4. The simulated and calculated position and pose error curves are obtained by using ADAMS and MATLAB.

Generally, the value of each error source of the parallel mechanism meets the normal distribution [32, 33]. The input error δl_i is set to follow the $N(0, 0.01)$ distribution, and the rest of the errors obey the $N(0, 0.2)$ distribution. The motion trajectory of the moving platform is given.

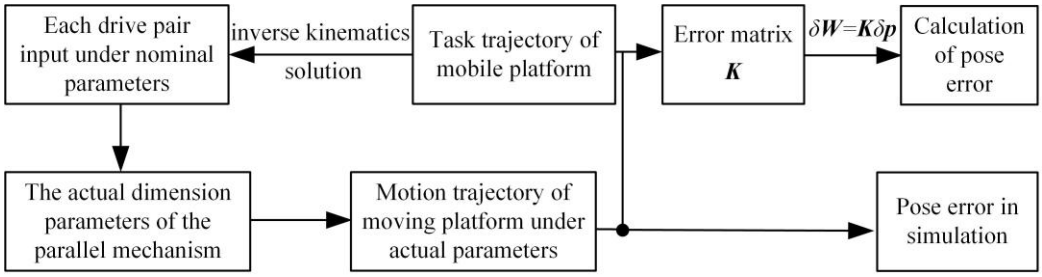

Figure 4 Analysis process of the influence of geometric errors on dynamic accuracy

$$\begin{cases} x = 10\sin(0.4\pi t), & \beta = -0.1\pi \\ y = 10\sin(0.4\pi t), & \gamma = 0 \\ z = 500 - 5\sin(0.4\pi t) \end{cases} \tag{7}$$

By applying the inverse kinematics transformation of the parallel mechanism, the error mapping matrix $\boldsymbol{K}$ can be calculated. The calculated position and pose error curve can be obtained by substituting $\boldsymbol{K}$ into Eq. (5). Comparing with the simulation results is shown in Fig. 5.

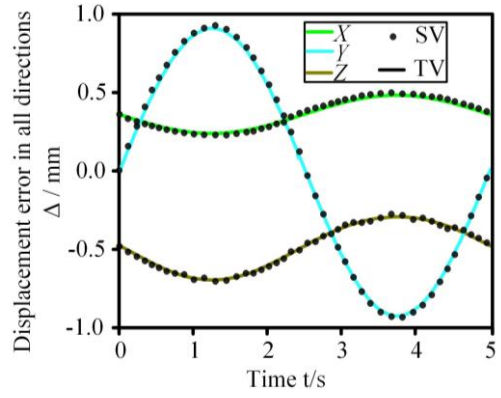

(a) Position displacement error of moving platform

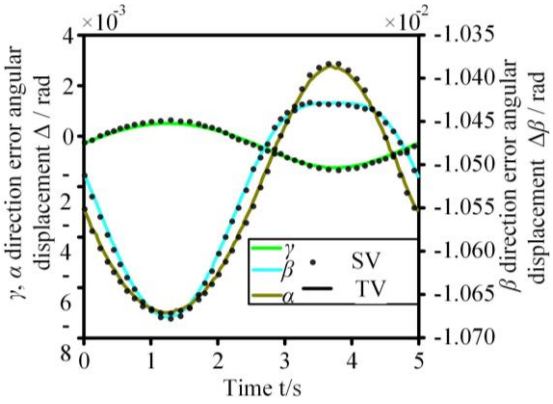

(b) Pose displacement error of moving platform

Figure 5 Position and posture error sensitivity

As shown in Fig. 5, there is a certain deviation between the simulation result and the theoretical calculation, because the theoretical position and pose of the moving platform is used for calculating the error mapping matrix $\boldsymbol{K}$. When t=3.8s, the position errors along the $\boldsymbol{X}$-axis and $\boldsymbol{Y}$-axis directions reach the maximum values, while the pose error along the γ and α directions reach the maximum values. When t=1.3s, the position error along the $\boldsymbol{Z}$-axis reaches the maximum value, while the pose error along the β direction reaches the maximum value. The simulation results show that the geometric errors have a greater impact on the dynamic accuracy of the parallel mechanism. If not taken into account, it will seriously degenerate the performance of the parallel mechanism.

2.3 Calibration of geometric errors

According to the structural characteristics and driving mode of the 5-PSS/UPU parallel mechanism, a vector calibration algorithm based on the inverse position solution is used to calibrate the geometric error. The positioning accuracy of actuator can be ignored because the high-precision screw module has high repetitive position accuracy.

When considering the existence of errors, Eq. (1) can be written as

$$\begin{aligned} &\boldsymbol{D} + {}^{O}_{D}\boldsymbol{R}\left({}^{D}\boldsymbol{C}_i + \delta\,{}^{D}\boldsymbol{C}_i\right) \\ &= \left(\boldsymbol{A}_i + \delta\boldsymbol{A}_i\right) + \left(l_i + \delta l_i\right)\left(\boldsymbol{s}_i + \delta\boldsymbol{s}_i\right) + \left(L_i + \delta L_i\right)\boldsymbol{n}_i \end{aligned} \tag{8}$$

$\boldsymbol{D}$, ${}^{O}_{D}\boldsymbol{R}$ and $\boldsymbol{n}_i$ in Eq. (1) and Eq. (8) are identical in the same position and pose of the moving platform. After subtracting the two Eqs, the new equation is taken the dot products of both sides with vector $\boldsymbol{n}_i^{\mathrm{T}}$ as.

$$\boldsymbol{n}_i^{\mathrm{T}} \cdot {}^{O}_{D}\boldsymbol{R} \cdot \delta\,{}^{D}\boldsymbol{C}_i = \boldsymbol{n}_i^{\mathrm{T}} \cdot \delta\boldsymbol{A}_i + l_i\boldsymbol{n}_i^{\mathrm{T}} \cdot \delta\boldsymbol{s}_i + \delta L_i \tag{9}$$

Error sources $\delta\,{}^{D}\boldsymbol{C}_i$ and $\delta\boldsymbol{s}_i$ contain two independent error parameters. There are eight unknown error parameters in Eq. (9), so 5 branches include 40 unknown error parameters. Measuring posture can list 5 equations, thereby at least 8 groups of different mechanism position parameters, which are required to be different as large as possible between them, need to be measured to reduce the coupling effect of each error parameter. According to actual condition, it is also possible to measure several sets of position parameters while taking the average of the obtained errors obtains higher calibration accuracy.

The vector calibration algorithm is used to identify the parameters of the 5-PSS/UPU parallel mechanism. Adopting Eq. (5) and the error data of Fig. 5 as the actual size error, different position parameters can be obtained in terms of the actual structure size of the parallel mechanism,

which is used to replace the actual measured position parameters. The actual structure size parameters and mechanism size parameters obtained by identification are regarded as the input and output of the Calculation of vector calibration. Finally, comparing the input with output parameters evaluates the accuracy of the calibration algorithm. The active branch chain 1 of the parallel mechanism is selected for simulation calculation, and the pose parameters given by the actual structure size of the parallel mechanism (Table 1).

Table 1 Posture parameter samples

Sample number	γ (rad)	β (rad)	n_{1x} (mm)	n_{1y} (mm)	n_{1z} (mm)	l_1 (mm)
1	0.0217	0.0217	-0.5622	0.0093	0.8270	8.6538
2	0.0468	0.0468	-0.5354	0.0196	0.8444	19.6880
3	0.0672	0.0672	-0.5127	0.0280	0.8581	29.3322
4	0.0811	0.0811	-0.4970	0.0337	0.8671	36.2070
5	0.0871	0.0871	-0.4902	0.0362	0.8709	39.2365
6	0.0845	0.0845	-0.4931	0.0351	0.8692	37.9234
7	0.0737	0.0737	-0.5055	0.0307	0.8623	32.4848
8	0.0556	0.0556	-0.5257	0.0233	0.8504	23.7929

As shown in Table 2, the error values were obtained by the vector calibration algorithm according to formula (9). We can see that most of the calibration values obtained by the vector calibration method have an accuracy of more than 90%, which indicates the correctness and effectiveness of the calibration method. The reason for affecting the accuracy is that the driving input error is ignored. In addition, it is noteworthy that sensors also have some accuracy problems in real situation, so the accuracy of the actual calibration results will be lower than that of the simulation results. On the whole, the vector calibration method is generally effective for the calibration of 5-PSS/UPU parallel mechanism.

Table 2 Calibration results

Error source	Real value	Calibration value	Accuracy rate
δL_1	0.255	0.239	93.42%
$\delta^D C_{1x}$	-0.144	-0.130	90.06%
$\delta^D C_{1y}$	0.00542	0.00601	88.89%
$\delta^D C_{1z}$	0.0143	0.0155	91.61%
δA_{1x}	-0.103	-0.110	92.50*
δA_{1y}	-0.234	-0.221	94.65%
$\delta\theta_1$	0.237	0.247	95.44%
$\delta\varphi_1$	0.116	0.108	93.37%

To further verify the effectiveness of calibration for improving dynamic accuracy, the position and pose errors of the moving platform before and after the calibration were compared. The specific process is shown in Figure 6, and the error calibration values of all error sources obtained by the vector calibration algorithm are shown in Fig. 7.

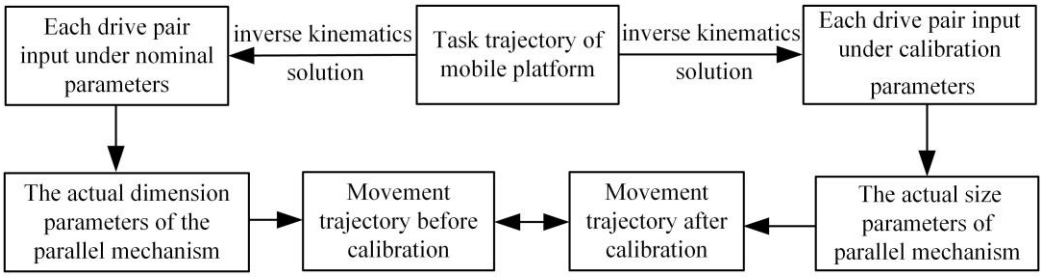

Figure 6 Comparison process of posture error before and after calibration

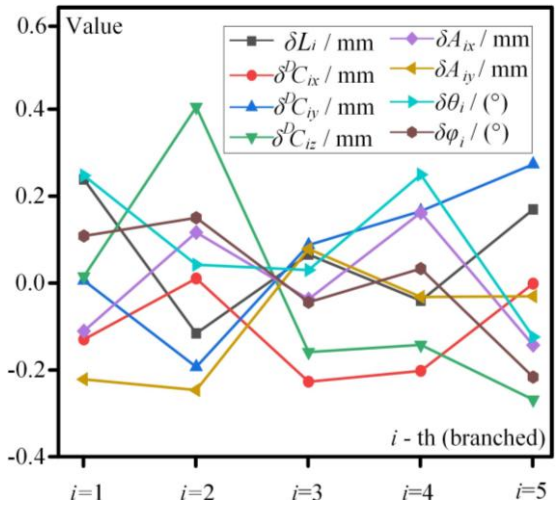

Figure 7 Error calibration values

The moving position and pose errors of the moving platform after calibration can be calculated along the trajectory in Eq. (7). As shown in Fig. 8, the calibrated dynamic accuracy of the parallel mechanism has been greatly increased. In the fixed coordinate system, the position errors along the *X*-axis, *Y*-axis and *Z*-axis directions are reduced by 93.5%, 92.5%, and 91.7% respectively, while the angle errors around the *X*-axis, *Y*-axis and *Z*-axis directions are reduced by 93.6%, 91.2%, and 86.8% respectively. It illustrates that the necessity of calibration of the parallel mechanism before it is put into work. On the other hand, the reliability of the proposed calibration algorithm has also been illustrated.

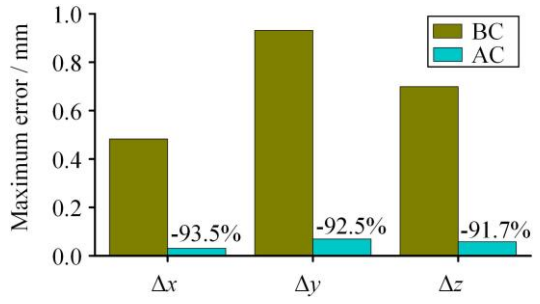

(a) Maximum position errors

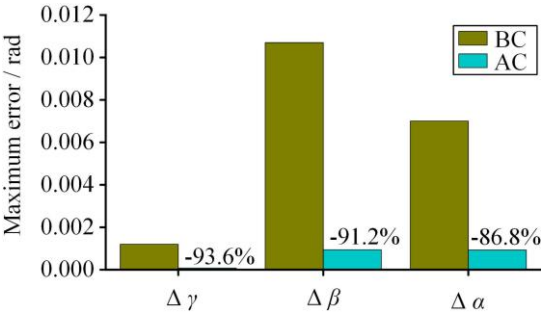

(b) Maximum position errors

Figure 8 Comparison of posture errors before and after calibration

3 Analysis of dynamic accuracy

3.1 Dynamic modeling of rigid-flexible coupling

Before establishing elastodynamic modeling of parallel mechanisms, two assumptions are proposed: one is that the displacement of the mechanism obtained by elastodynamic analysis is much smaller than that of the rigid body dynamics. Second, whilst there is a coupling effect between the rigid and elastic motion of the mechanism, the coupling relationship terms between them can be ignored in terms of a mechanism with less flexibility [34].

3.1.1 Spatial beam element model

The five-branch links of the parallel mechanism are identically regarded as flexible parts, while the moving platform, fixed base, modules and each motion pair are all regarded as rigid bodies. Meanwhile, the influence of clearance of the spherical pair is ignored. The flexible link is regarded as the spatial beam element, as shown in Fig. 9. The coordinate system $o_{ij}-x_{ij}y_{ij}z_{ij}$ of beam element is introduced where the subscript i and j represent the i-th branch link and the j-th element. Each element has 2 nodes where each node has 9 elastic displacement degrees of freedom. The generalized coordinate $\boldsymbol{\delta}_{ij}$ of the spatial beam element can be expressed as

$$\boldsymbol{\delta}_{ij}=[\delta_{ij1},\delta_{ij2},...,\delta_{ij17},\delta_{ij18}]^{\mathrm{T}} \tag{10}$$

where $\delta_{ij1}\sim\delta_{ij3}$ and $\delta_{ij10}\sim\delta_{ij12}$ represent element node displacements. $\delta_{ij4}\sim\delta_{ij6}$ and $\delta_{ij13}\sim\delta_{ij15}$ represent element node rotation angles, $\delta_{ij7}\sim\delta_{ij9}$ and $\delta_{ij16}\sim\delta_{ij18}$ represent element node curvatures.

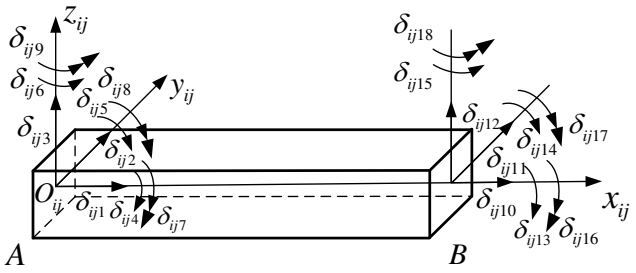

Figure 9 Spatial beam element model

The angular displacement around the axis is interpolated by a cubic difference function. The displacement and rotation angle in the other directions are interpolated by a quintic function. If $W_x(x_{ij},t)$, $W_y(x_{ij},t)$, $W_z(x_{ij},t)$, $\varphi_x(x_{ij},t)$, $\varphi_y(x_{ij},t)$ and $\varphi_z(x_{ij},t)$ are used to denote the elastic displacement and elastic angular displacement of any point in the element along x-axis, y-axis and z-axis directions, other parameters can be represented by generalized coordinate $\boldsymbol{\delta}_{ij}$.

According to the boundary conditions of the beam element and the corresponding interpolation function, the displacement functions of the beam element can be expressed as

$$\begin{cases}\boldsymbol{W}(x_{ij},t)=\left[\boldsymbol{N}_{ij1}^{\mathrm{T}}\boldsymbol{\delta}_{ij}\quad \boldsymbol{N}_{ij2}^{\mathrm{T}}\boldsymbol{\delta}_{ij}\quad \boldsymbol{N}_{ij3}^{\mathrm{T}}\boldsymbol{\delta}_{ij}\right]^{\mathrm{T}}\\ \boldsymbol{\varphi}(x_{ij},t)=\left[\boldsymbol{N}_{ij4}^{\mathrm{T}}\boldsymbol{\delta}_{ij}\quad \boldsymbol{N}_{ij3}^{\mathrm{T}}\boldsymbol{\delta}_{ij}\quad \boldsymbol{N}_{ij2}^{\mathrm{T}}\boldsymbol{\delta}_{ij}\right]^{\mathrm{T}}\end{cases} \tag{11}$$

where $\boldsymbol{N}_{ij1}$, $\boldsymbol{N}_{ij2}$, $\boldsymbol{N}_{ij3}$ and $\boldsymbol{N}_{ij4}$ represent the vector matrix obtained by interpolation.

$$\begin{aligned}\boldsymbol{\delta}_{rij}=\big[&x_{\mathrm{A}}\quad y_{\mathrm{A}}\quad z_{\mathrm{A}}\quad \theta_x\quad \theta_y\quad \theta_z\quad 0\quad 0\quad 0\\ &x_{\mathrm{B}}\quad y_{\mathrm{B}}\quad z_{\mathrm{B}}\quad \theta_x\quad \theta_y\quad \theta_z\quad 0\quad 0\quad 0\big]^{\mathrm{T}}\end{aligned} \tag{12}$$

where $x_{\mathrm{A(B)}}$, $y_{\mathrm{A(B)}}$ and $z_{\mathrm{A(B)}}$ represent the rigid body displacements of the element nodes $A(B)$ along the X-axis, Y-axis and Z-axis directions. θ_x, θ_y, and θ_z represent the rigid body rotation angle of the two element nodes around the X-axis, Y-axis and Z-axis.

Assuming that the mass of each element is concentrated on the axis, the kinetic energy of the element can be expressed as

$$\begin{aligned}T_{ij}=&\frac{1}{2}\int_0^{L_{ij}}\rho S\left[\left(\frac{d\omega_{ax}(x_{ij},t)}{dt}\right)^2+\left(\frac{d\omega_{ay}(x_{ij},t)}{dt}\right)^2+\left(\frac{d\omega_{az}(x_{ij},t)}{dt}\right)^2\right]dx\\ &+\frac{1}{2}\int_0^{L_{ij}}\rho I_p\left(\frac{d\varphi_{ax}(x_{ij},t)}{dt}\right)^2dx=\frac{1}{2}\left(\dot{\boldsymbol{\delta}}_{ij}+\dot{\boldsymbol{\delta}}_{rij}\right)^{\mathrm{T}}\boldsymbol{M}_e\left(\dot{\boldsymbol{\delta}}_{ij}+\dot{\boldsymbol{\delta}}_{rij}\right)\end{aligned} \tag{13}$$

where ρ and S are the material density and cross-sectional area of the element. I_x represents the polar inertia moment of the element cross-section along the X-axis direction.

If the shear deformation of the beam element and the coupling between the axial and the lateral displacement are ignored, the deformation potential energy of the spatial

beam element can be expressed as

$$V_{ij}=\frac{1}{2}E\int_0^{L_{ij}}[(\frac{\partial\omega_x(x_{ij},t)}{\partial x^2})^2+(\frac{\partial\omega_y(x_{ij},t)}{\partial x^2})^2+(\frac{\partial\omega_z(x_{ij},t)}{\partial x^2})^2]dx$$
$$+\frac{1}{2}\int_0^{L_{ij}}GI_x\left(\frac{\partial\varphi_x(x_{ij},t)}{\partial x}\right)^2dx=\frac{1}{2}\boldsymbol{\delta}_{ij}^{\mathrm{T}}\boldsymbol{K}_{ij}\boldsymbol{\delta}_{ij} \tag{14}$$

with $\boldsymbol{K}_{ij}=E\int_0^{L_{ij}}(S\ddot{\boldsymbol{N}}_1\boldsymbol{N}_1^{\mathrm{T}}+I_z\ddot{\boldsymbol{N}}_2\boldsymbol{N}_2^{\mathrm{T}}+I_y\ddot{\boldsymbol{N}}_3\boldsymbol{N}_3^{\mathrm{T}})dx$
$+GI_x\int_0^{L_{ij}}\ddot{\boldsymbol{N}}_4\boldsymbol{N}_4^{\mathrm{T}}dx$

where I_y and I_z represent the polar inertia moments of the element cross-section of the element along the *Y*-axis and *Z*-axis. $\boldsymbol{K}_{ij}$ denotes the stiffness matrix of the element.

According to the Lagrange dynamics equation [35], by applying the kinetic energy and deformation potential energy of the space beam element, the elastodynamic equation of the element in the local coordinate system can be expressed as

$$\boldsymbol{M}_{ij}\ddot{\boldsymbol{\delta}}_{ij}+\boldsymbol{K}_{ij}\boldsymbol{\delta}_{ij}=\boldsymbol{F}_{ij}+\boldsymbol{P}_{ij}+\boldsymbol{Q}_{ij} \tag{15}$$

with $\boldsymbol{M}_{ij}=\rho S\int_0^{L_{ij}}\boldsymbol{N}_\omega\boldsymbol{N}_\omega^{\mathrm{T}}dx+\rho I_x\int_0^{L_{ij}}\boldsymbol{N}_1\boldsymbol{N}_1^{\mathrm{T}}dx$,

$\boldsymbol{N}_\omega=\begin{bmatrix}\boldsymbol{N}_1 & \boldsymbol{N}_2 & \boldsymbol{N}_3\end{bmatrix}$.

where $\boldsymbol{M}_{ij}$ denotes the mass matrix of the element. $\boldsymbol{F}_{ij}$ denotes the generalized external force term including force and torque. $\boldsymbol{P}_{ij}$ represents the interaction force term caused by the connection of the beam element. $\boldsymbol{Q}_{ij}$ is the rigid body inertial force term.

To facilitate elastic modelling, the elastodynamic equations in the local coordinate system are converted to the base coordinate system, as shown in Fig. 10. The generalized coordinates $\bar{\boldsymbol{\delta}}_{ij}$ in the base coordinate system can be expressed as

$$\bar{\boldsymbol{\delta}}_{ij}=\bar{\boldsymbol{R}}_{ij}\boldsymbol{\delta}_{ij} \tag{16}$$

where $\bar{\boldsymbol{R}}_{ij}=diag\left(\boldsymbol{R}_{ij},\boldsymbol{R}_{ij},\boldsymbol{R}_{ij},\boldsymbol{R}_{ij},\boldsymbol{R}_{ij},\boldsymbol{R}_{ij}\right)$, $\boldsymbol{R}_{ij}$ represents the transformation matrix from the local coordinate system to the base coordinate system of link.

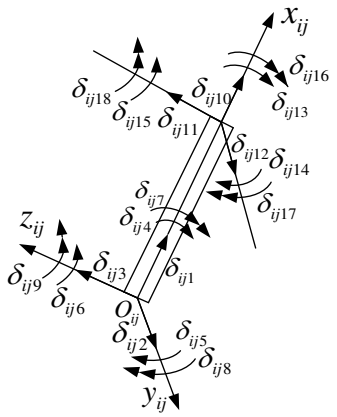

(a) Element generalized coordinates in link coordinate system

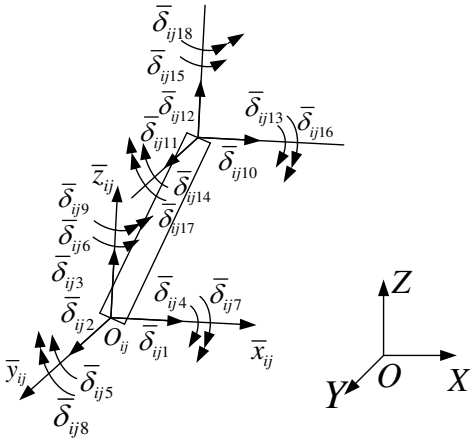

(b) Element generalized coordinates in base coordinate system

Figure 10 Unit coordinate system transformation

From Eq. (16) we can obtain the relational expressions with the first and second derivatives of $\boldsymbol{\delta}_{ij}$

$$\begin{cases}\dot{\bar{\boldsymbol{\delta}}}_{ij}=\bar{\boldsymbol{R}}_{ij}\dot{\boldsymbol{\delta}}_{ij}+\dot{\bar{\boldsymbol{R}}}_{ij}\bar{\boldsymbol{\delta}}_{ij}\\ \ddot{\bar{\boldsymbol{\delta}}}_{ij}=\bar{\boldsymbol{R}}_{ij}\ddot{\boldsymbol{\delta}}_{ij}+2\dot{\bar{\boldsymbol{R}}}_{ij}\dot{\boldsymbol{\delta}}_{ij}+\ddot{\bar{\boldsymbol{R}}}_{ij}\bar{\boldsymbol{\delta}}_{ij}\end{cases} \tag{17}$$

By substituting Eq. (17) into Eq. (15), the elastodynamic equation of the element in the base coordinate system can be expressed as

$$\bar{\boldsymbol{M}}_{ij}\ddot{\bar{\boldsymbol{\delta}}}_{ij}+\bar{\boldsymbol{C}}_{ij}\dot{\bar{\boldsymbol{\delta}}}_{ij}+\bar{\boldsymbol{K}}_{ij}\bar{\boldsymbol{\delta}}_{ij}=\bar{\boldsymbol{Q}}_{ij} \tag{18}$$

where $\bar{\boldsymbol{M}}_{ij}=\bar{\boldsymbol{R}}_{ij}^{\mathrm{T}}\boldsymbol{M}_{ij}\bar{\boldsymbol{R}}_{ij}$, $\bar{\boldsymbol{C}}_{ij}=2\bar{\boldsymbol{R}}_{ij}^{\mathrm{T}}\boldsymbol{M}_{ij}\dot{\bar{\boldsymbol{R}}}_{ij}$,

$\bar{\boldsymbol{K}}_{ij}=\bar{\boldsymbol{R}}_{ij}^{\mathrm{T}}\boldsymbol{M}_{ij}\ddot{\bar{\boldsymbol{R}}}_{ij}+\bar{\boldsymbol{R}}_{ij}^{\mathrm{T}}\boldsymbol{K}_{ij}\bar{\boldsymbol{R}}_{ij}$, $\bar{\boldsymbol{Q}}_{ij}=\bar{\boldsymbol{R}}_{ij}^{\mathrm{T}}\left(\boldsymbol{F}_{ij}+\boldsymbol{P}_{ij}+\boldsymbol{Q}_{ij}\right)$.

3.1.2 Elastodynamic modeling of fixed-length link

The fixed-length link is regarded as a flexible rod while the rest are assumed to be rigid parts. As shown in Fig. 11, the link is divided into *n* elements, which are numbered 1, 2, ..., *n*+1 in sequence. Each element is connected adjacently in turn. The elastic displacement of the right end of the *j*-th element is consistent with that of the left end of the (*j*+1)-th unit, 1≤*j*≤n-1.

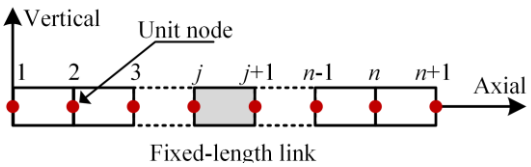

Figure 11 Division of the link unit

Connecting the left and right ends of the fixed-length link are spherical pairs, thereby the curvature of the end beam element is 0, i. e. $\bar{\delta}_{(i1)7}=\bar{\delta}_{(i1)8}=\bar{\delta}_{(i1)9}=0$, $\bar{\delta}_{(in)16}=\bar{\delta}_{(in)17}=\bar{\delta}_{(in)18}=0$. Synthetically, the generalized coordinate $\boldsymbol{q}_i$ of the link can be obtained from the displacement relationship between the elements.

$$\boldsymbol{q}_i = [\bar{\delta}_{(i1)1}, \bar{\delta}_{(i1)2}, \mathrm{L}\ , \bar{\delta}_{(i1)6}, \bar{\delta}_{(i2)1}, \bar{\delta}_{(i2)2}, \mathrm{L}\ , \bar{\delta}_{(in)1}, \bar{\delta}_{(in)2}, \mathrm{L}\ , \bar{\delta}_{(in)15}] \tag{19}$$

The relationship between $\boldsymbol{q}_i$ and $\bar{\boldsymbol{\delta}}_{ij}$ can be expressed as

$$\bar{\boldsymbol{\delta}}_{ij} = \bar{\boldsymbol{A}}_{ij}\boldsymbol{q}_i \tag{20}$$

where

$$\bar{\boldsymbol{A}}_{ij} = \begin{cases} \left[\bar{\boldsymbol{B}}_{18\times15} \quad \boldsymbol{0}_{18\times(9n-12)}\right] & (j=1) \\ \left[\boldsymbol{0}_{18\times(9j-12)} \quad \boldsymbol{E}_{18} \quad \boldsymbol{0}_{18\times(9n-9j-3)}\right] & (j=2,3\mathrm{L}\ n-1) \\ \left[\boldsymbol{0}_{18\times(9n-12)} \quad \bar{\boldsymbol{C}}_{18\times15}\right] & (j=n) \end{cases}$$

$$\bar{\boldsymbol{B}}_{18\times15} = \begin{bmatrix} \boldsymbol{E}_6 & \boldsymbol{0}_{6\times9} \\ \boldsymbol{0}_{3\times6} & \boldsymbol{0}_{3\times9} \\ \boldsymbol{0}_{9\times6} & \boldsymbol{E}_9 \end{bmatrix} \qquad \bar{\boldsymbol{C}}_{18\times15} = \begin{bmatrix} \boldsymbol{E}_{15} \\ \boldsymbol{0}_{3\times15} \end{bmatrix}$$

By substituting Eq. (22) into Eq. (20) and taking the dot products of both sides with vector $\bar{\boldsymbol{A}}_{ij}$ to obtain the element elastodynamic equation of the link in the base coordinate system $\{O\}$.

$$\boldsymbol{M}_{ij}^i \ddot{\boldsymbol{q}}_i + \boldsymbol{C}_{ij}^i \dot{\boldsymbol{q}}_i + \boldsymbol{K}_{ij}^i \boldsymbol{q}_i = \boldsymbol{Q}_{ij}^i \tag{21}$$

where $\boldsymbol{M}_{ij}^i = \bar{\boldsymbol{A}}_{ij}^{\mathrm{T}} \bar{\boldsymbol{M}}_{ij} \bar{\boldsymbol{A}}_{ij}$, $\boldsymbol{C}_{ij}^i = \bar{\boldsymbol{A}}_{ij}^{\mathrm{T}} \bar{\boldsymbol{C}}_{ij} \bar{\boldsymbol{A}}_{ij}$, $\boldsymbol{K}_{ij}^i = \bar{\boldsymbol{A}}_{ij}^{\mathrm{T}} \bar{\boldsymbol{K}}_{ij} \bar{\boldsymbol{A}}_{ij}$, $\boldsymbol{Q}_{ij}^i = \bar{\boldsymbol{A}}_{ij}^{\mathrm{T}} \bar{\boldsymbol{Q}}_{ij}$.

The elastodynamic equation of the link can be obtained by superposing the elastodynamic equation of each element.

$$\boldsymbol{M}^i \ddot{\boldsymbol{q}}_i + \boldsymbol{C}^i \dot{\boldsymbol{q}}_i + \boldsymbol{K}^i \boldsymbol{q}_i = \boldsymbol{Q}^i \tag{22}$$

where $\boldsymbol{M}^i = \sum_{nj=1}^{n} \boldsymbol{M}_{ij}^i$, $\boldsymbol{C}^i = \sum_{j=1}^{n} \boldsymbol{C}_{ij}^i$, $\boldsymbol{K}^i = \sum_{j=1}^{n} \boldsymbol{K}_{ij}^i$, $\boldsymbol{Q}^i = \sum_{j=1}^{n} \boldsymbol{Q}_{ij}^i$.

3.1.3 Kinematics and dynamics constraint equation

The kinematic constraint of the system is the deformation coordination condition. Compared with the five fixed-length links, the moving platform can be regarded as a rigid body due to relatively larger rigidity. In this parallel mechanism, the displacement of the hinge point of the fixed-length link connected to the moving platform is consistent with that of the corresponding point of the moving platform, as shown in Fig. 12.

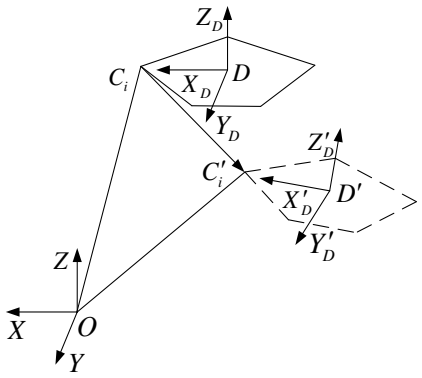

Figure 12 Constraints of system kinematics

The elastic deformation of the link makes the center point of the moving platform move from the original point O_D to the point O'_D. The three position and pose changes caused by the movable platform are expressed as $[\delta x_D, \delta y_D, \delta z_D, \delta\alpha_D, \delta\beta_D, \delta\gamma_D]$, which is abbreviated as $\boldsymbol{q}_D = [q_{D1}, q_{D2}, q_{D3}, q_{D4}, q_{D5}, q_{D6}]$ where $q_{D1}=\delta x_D$, $q_{D2}=\delta y_D$, $q_{D3}=\delta z_D$, $q_{D4}=\delta\gamma_D$, $q_{D5}=\delta\beta_D$ and $q_{D6}=\delta\alpha_D$. δx_D, δy_D, δz_D, $\delta\alpha_D$, $\delta\beta_D$ and $\delta\gamma_D$ are small variables, which can be approximated as according to Taylor and McLaughlin formulas.

$$\begin{cases} \sin\delta\alpha_D \approx \delta\alpha_D,\ \sin\delta\beta_D \approx \delta\beta_D,\ \sin\delta\gamma_D \approx \delta\gamma_D \\ \cos\delta\alpha_D \approx 1,\ \cos\delta\beta_D \approx 1,\ \cos\delta\gamma_D \approx 1 \end{cases} \tag{23}$$

The transformation matrix from coordinate system $\{D' - X'_D Y'_D Z'_D\}$ to $\{D - X_D Y_D Z_D\}$ can be expressed as $\Delta\boldsymbol{T}$. The transformation matrix ${}_D^O\boldsymbol{T}'$ from the coordinate system $\{D' - X'_D Y'_D Z'_D\}$ to the base coordinate system can be expressed as ${}_D^O\boldsymbol{T}' = \Delta\boldsymbol{T}\,{}_D^O\boldsymbol{T}$. The position of each hinge point on the moving platform relative to the moving platform is always fixed. The expression of C'_i in the base coordinate system can be expressed as

$$\begin{bmatrix} \boldsymbol{q}'_{Ci} \\ 1 \end{bmatrix} = \Delta\boldsymbol{T} \begin{bmatrix} \boldsymbol{q}_{Ci} \\ 1 \end{bmatrix} = \Delta\boldsymbol{T} \begin{bmatrix} \boldsymbol{J}_{ci}\boldsymbol{q}_D \\ 1 \end{bmatrix} \tag{24}$$

where $\boldsymbol{q}_{Ci}$ is the elastic displacement of the hinge. $\boldsymbol{J}_{Ci}$ denotes the kinematic constraint matrix. $\boldsymbol{q}_D$ represents the pose changes of the moving platform caused by elastic deformation.

Eq. (24) is the kinematic constraint equation of the 5-PSS/UPU parallel mechanism. Meanwhile, the parallel mechanism also needs to meet the dynamic constraint equation, i.e. the external force and inertial force of the moving platform must be balanced with the force exerted by the fixed-length link on the moving platform. Ignoring the coupling relationship between the rigid body motion and elastic motion of the moving platform, the dynamic constraint equation of the moving platform can be expressed as

$$\boldsymbol{M}_D \ddot{\boldsymbol{q}}_{aD} = \boldsymbol{F}_i + \boldsymbol{F}_w \tag{25}$$

where $\boldsymbol{M}_D$ is mass matrix of the moving platform. $\ddot{\boldsymbol{q}}_{aD}$ denotes the acceleration array of the moving platform. $\boldsymbol{F}_i$ is the combined force array of the branch-chain on the moving platform, $\boldsymbol{F}_w$ is the external force array on the moving platform.

The dynamic constraint equation in term of $\ddot{\boldsymbol{q}}_{aD} = \ddot{\boldsymbol{q}}_D + \ddot{\boldsymbol{q}}_{mD}$ can be rewritten as:

$$\boldsymbol{M}_D \ddot{\boldsymbol{q}}_D = \boldsymbol{Q}_D \tag{26}$$

where $\boldsymbol{Q}_D = \boldsymbol{F}_i + \boldsymbol{F}_w - \boldsymbol{M}_D \ddot{\boldsymbol{q}}_{mD}$.

3.1.4 Elastic dynamics equation of parallel mechanism system

According to the elastodynamic equations of each branch

chain, the kinematics and dynamics constraint relations of each component of the system, the elastodynamic equations of each link are assembled. To facilitate the analysis, a generalized coordinate of branch chain $\hat{\boldsymbol{q}}_i\left(i=1,2,3,4,5\right)$ is defined as

$$\begin{aligned}\hat{\boldsymbol{q}}_i=\big[&\bar{\delta}_{(i1)1},\bar{\delta}_{(i1)2},\mathrm{L}\ ,\bar{\delta}_{(i1)6},\bar{\delta}_{(i2)1},\bar{\delta}_{(i2)2},\mathrm{L}\ ,\bar{\delta}_{(in)1},\mathrm{L}\ ,\bar{\delta}_{(in)9},\\&\bar{\delta}_{(in)13},\bar{\delta}_{(in)14},\bar{\delta}_{(in)15},q_{D1},q_{D2},q_{D3},q_{D4},q_{D5},q_{D6}\big]^{\mathrm{T}}\end{aligned} \tag{27}$$

The relation equation $\boldsymbol{q}_i=\hat{\boldsymbol{R}}_i\hat{\boldsymbol{q}}_i$ between $\hat{\boldsymbol{q}}_i$ and $\boldsymbol{q}_i$ can be obtained from the kinematics constraint relation equation. Substituting the equation into Eq. (22), the new equation is taken the dot products of both sides with vector $\hat{\boldsymbol{R}}_i^{\mathrm{T}}$ as

$$\boldsymbol{M}_i\ddot{\hat{\boldsymbol{q}}}_i+\boldsymbol{C}_i\dot{\hat{\boldsymbol{q}}}_i+\boldsymbol{K}_i\hat{\boldsymbol{q}}_i=\boldsymbol{Q}_i \tag{28}$$

Meanwhile, to facilitate the assembly of the system equations, the generalized system coordinate $\hat{\boldsymbol{q}}_i$ and $\boldsymbol{q}_i$ can be written as

$$\begin{cases}\hat{\boldsymbol{q}}_i=[\hat{\boldsymbol{q}}_i^{\mathrm{T}}\quad \boldsymbol{q}_D]^{\mathrm{T}}\\ \boldsymbol{q}=\big[\hat{\boldsymbol{q}}_1^{\mathrm{T}},\hat{\boldsymbol{q}}_2^{\mathrm{T}},\hat{\boldsymbol{q}}_3^{\mathrm{T}},\hat{\boldsymbol{q}}_4^{\mathrm{T}},\hat{\boldsymbol{q}}_5^{\mathrm{T}},\boldsymbol{q}_D^{\mathrm{T}}\big]^{\mathrm{T}}\end{cases} \tag{29}$$

The mapping relation between generalized system coordinates $\boldsymbol{q}$ and $\hat{\boldsymbol{q}}_i$ can be written as:

$$\hat{\boldsymbol{q}}_i=\boldsymbol{R}_i\boldsymbol{q} \tag{30}$$

By assembling and superposing all the elastodynamic equations of the branch links as well as considering the effect of the system damping, the elastodynamic equations of the whole system of the 5-PSS/UPU parallel mechanism in the base coordinate system can be expressed as

$$\boldsymbol{M}\ddot{\boldsymbol{q}}+\boldsymbol{C}\dot{\boldsymbol{q}}+\boldsymbol{K}\boldsymbol{q}=\boldsymbol{Q} \tag{31}$$

where $\boldsymbol{M}$ is the total mass matrix of the system. $\boldsymbol{C}$ is the coefficient matrix considering the damping effect. $\boldsymbol{K}$ is the total stiffness matrix of the system, $\boldsymbol{Q}$ is the generalized force matrix of the system.

3.2 Analysis of dynamic accuracy

The structure and material parameters of the 5-PSS/UPU parallel mechanism are shown in Table 3. The motion trajectory of the moving platform is given.

$$\begin{cases}x=0,\quad \beta=\pi/18\sin\left(2\pi t\right)\\ y=0,\quad \gamma=\pi/18\sin\left(2\pi t\right)\\ z=0.554+0.08\sin\left(\pi t\right)\end{cases} \tag{32}$$

The solution integration step is set to $\Delta t=0.001\mathrm{s}$. The solution time is $t=2\mathrm{s}$ and the Newmark method [36] is used to calculate the position and pose errors, velocity error and acceleration error of the moving platform caused by the elastic deformation of the branch rod, as shown in Fig. 13.

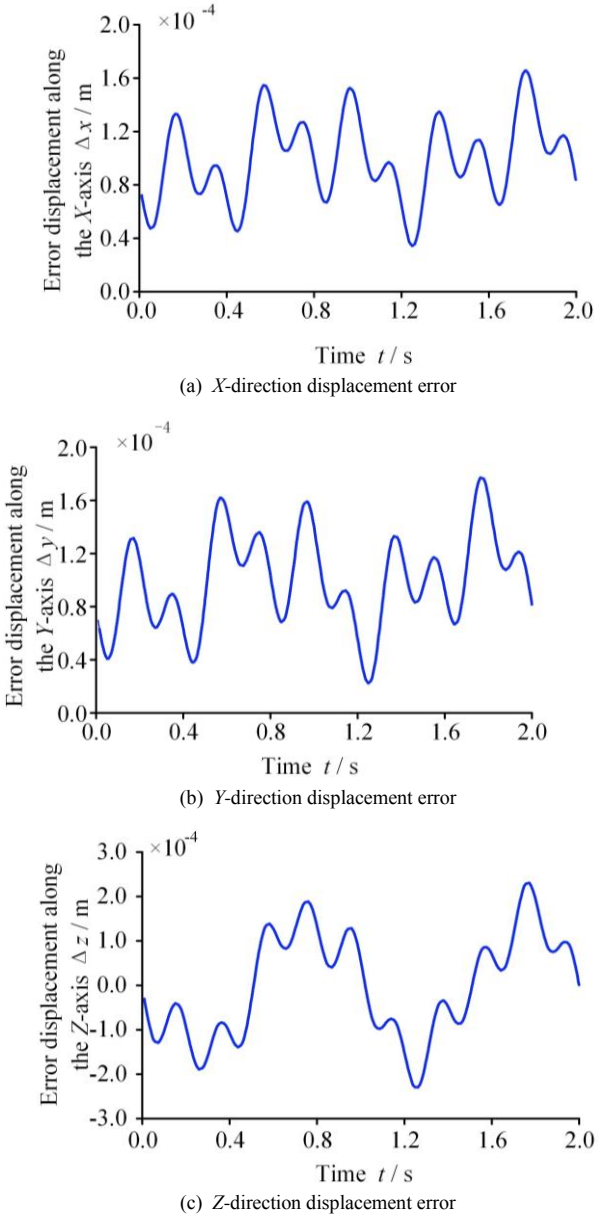

(a) X-direction displacement error

(b) Y-direction displacement error

(c) Z-direction displacement error

Figure 13 Position displacement error of moving platform

Obviously, it can be seen from Fig. 13 and Fig. 14 that the position and pose of the moving platform have produced relatively violent oscillations due to the elastic deformation of the branch link. These oscillations have greatly affected the dynamic accuracy of the moving platform. When moving time $t=1.772\mathrm{s}$, the moving platform produces the maximum displacement error along the X-axis and Y-axis directions. When the moving time $t=1.264\mathrm{s}$, the moving platform produces the maximum displacement error in the Z-axis direction. When the moving time $t=1.791\mathrm{s}$, the moving platform produces the maximum displacement error in the β direction. When the movement time $t=1.248\mathrm{s}$, the moving platform produces the maximum displacement error along the γ direction.

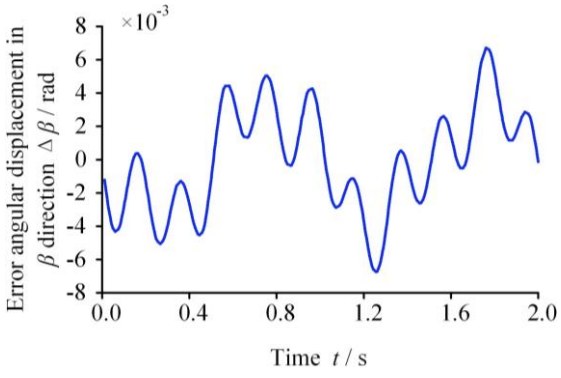

(a) β -angular displacement error

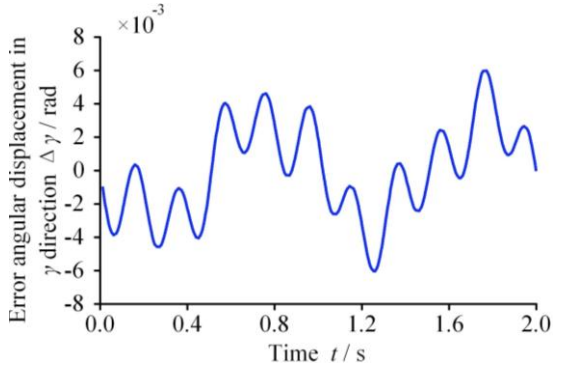

(b) γ -angular displacement error

Figure 14 Posture displacement error of moving platform

Table 3 Structure parameters of 5-PSS / UPU parallel mechanism

Parameter name	Value
Link length L_{BC}/mm	560
Link material density ρ_{BC} /kg·m^{-3}	2.7×10^{3}
Cross-sectional area of link S_{BC} /mm^{-2}	400π
Elastic modulus of link E_{BC} /Pa	0.7×10^{11}
Link shear modulus G_{BC} /Pa	2.7×10^{10}
Mobile platform quality m_D /kg	20

To quantitatively analyze the influence of factors, such as the cross-sectional area of the branch link, the elastic modulus and the mass of the moving platform, on the dynamic accuracy of the flexible parallel mechanism, the evaluation is obtained by calculating the corresponding influence index of dimensionless root mean square error [37], The influence index of dimensionless root mean square error can be written as

$$DRMSP(x)=\frac{RMS(x_{ai}-x_i)}{RMS(x_i)}\times100\% \tag{33}$$

where x_{ai} represents the output of the moving platform in real condition, x_i denotes the output of the moving platform in ideal condition. $RMS(x_{ai}-x_i)$ represents the root mean square error of the output of the moving platform in real condition. $RMS(x_i)$ represents the root mean square error of the output of the moving platform in ideal condition. Among them, $RMS(x_{ai}-x_i)=\sqrt{\frac{1}{N}\sum_{i=1}^{N}(x_{ai}-x_i)^2}$, $RMS(x_i)=\sqrt{\frac{1}{N}\sum_{i=1}^{N}x_i^{\,2}}$, N is the simulated sample size. To make the results more intuitive and representative, the dimensionless root mean square error influence index of the displacement, velocity and acceleration in the Z-axis direction of the centroid of the moving platform will be calculated.

It can be seen from Eq. (33) that the dynamic accuracy is proportional to the dimensionless root mean square error. In terms of the different conditions of the cross-sectional area, elastic modulus and moving platform mass of the branch link, the quantitative calculation of the non-dimensional root mean square error of the output of the parallel mechanism is shown in Fig. 16.

Fig. 16(a) shows that the non-dimensional root-mean -square error of the position, velocity and acceleration of the moving platform of the parallel mechanism are proportional to the cross-sectional area. When the cross-sectional area increases from 400 π mm^2 to 900 π mm^2, the dimensionless root-mean-square error influence indexes of displacement, velocity and acceleration decrease from 0.0284%, 5.6235% and 59.6772% to 0.0019%, 0.8277%, and 8.6590%, respectively. It shows that the larger cross-sectional area of the branch rod corresponds to the smaller output error of the mechanism and the higher dynamic accuracy.

Similarly, the non-dimensional root-mean-square error of the position, velocity and acceleration of the moving platform of the parallel mechanism are proportional to the elastic modulus, as shown in Fig. 16(b). When the elastic modulus increases from 70GPa to 206GPa, the dimensionless root-mean- square error influence indexes of displacement, velocity, and acceleration decrease from 0.0284%, 5.6235% and 59.6772% to 0.0029%, 0.7950% and 20.0719%, respectively. It illustrates that the larger elastic modulus of the branch rod corresponds to the smaller output error of the mechanism and the higher dynamic accuracy.

In Fig. 16(c), the non-dimensional root-mean-square error of the position, velocity and acceleration of the moving platform of the parallel mechanism are proportional to the mass of moving platform. When the mass of moving platform increases from 20kg to 60kg, the dimensionless root-mean-square error influence indexes of displacement, velocity, and acceleration increase from 0.0284%, 5.6235% and 59.6772% to 0.0708%, 13.6946% and 124.250%, respectively. It shows that the greater mass of the moving platform corresponds to the greater the output error of the mechanism, the more unstable the vibration amplitude of the mechanism and the lower dynamic accuracy.

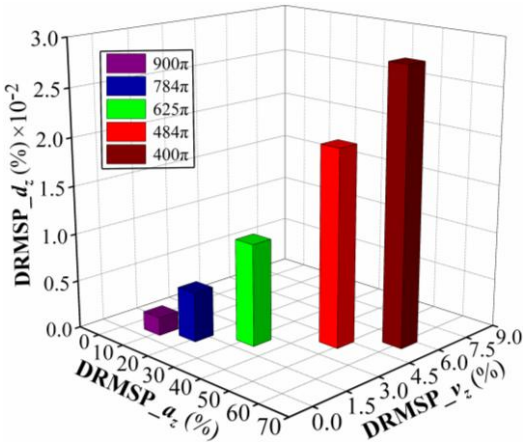

(a) cross-sectional area

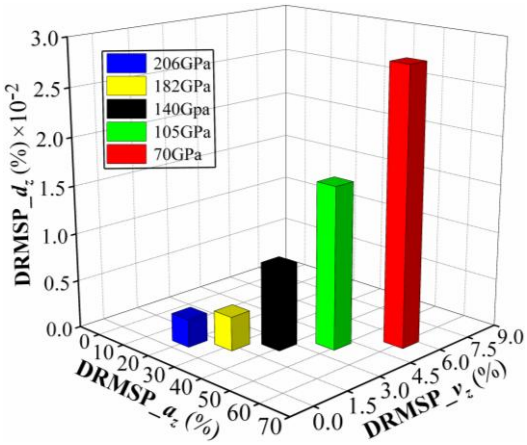

(b) elastic modulus

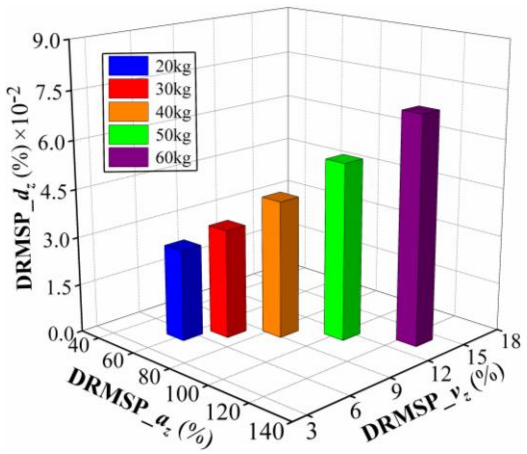

(c) moving platform quality

Fig. 16 Quantitative analysis of the output *DRMSP*(*x*)

4 Conclusion

Taking a 5-PSS/UPU parallel mechanism as an example, on the basis of an error model and the mapping law of geometric error to the dynamic accuracy, a vector calibration algorithm was proposed to reduce the position and pose error along the whole motion trajectory. The elastic dynamic model was established via analyzing the elastic deformation of the components. Furthermore, the effect of the flexibility of the components on the dynamic accuracy of the parallel mechanism was analyzed.

(1) The geometric error model is established by the closed chain vector method, and then the influence of each error source on the dynamic accuracy of the mechanism is analyzed. The simulation results show that the geometric error has a greater impact on the dynamic accuracy of the parallel mechanism.

(2) According to the structural and error characteristics of the parallel mechanism, a simple and efficient vector calibration method is proposed to obtain higher calibration accuracy. The position error along the x-axis, y-axis, and z-axis directions are reduced by 93.5%, 92.5%, 91.7% respectively, while the angle errors around the x-axis, y-axis, and z-axis directions are reduced by 93.6%, 91.2%, and 86.8% respectively.

(3) The elastic dynamics equation of the parallel mechanism is established by combining the finite element method with Lagrange method. Additionally, the Newmark direct integration method is used to solve it. The effects of the cross-sectional area, the elastic modulus and the mass of the moving platform of the branch connecting rod on the output of the moving platform are quantitatively analyzed.

(4) Numerical simulation results show that the cross-sectional area of the branch connecting rod and the elastic modulus are proportional to the dimensionless root mean square error of the output of the moving platform, while the mass of the moving platform is inverse proportional to the dimensionless root mean square error of the output of the moving platform.

Authors' contributions

The author' contributions are as follows: Y-BL was in charge of the whole trial; Z-SW and C-QC wrote the manuscript; T-TX, and BC assisted with sampling and laboratory analyses.

Author Details

[1] College of Mechanical Engineering, Zhejiang University of Technology, Hangzhou 310023, China

[2] Key Laboratory of E & M, Ministry of Education & Zhejiang Province, Zhejiang University of Technology, Hangzhou 310023, China.

Authors' Information

Yanbiao Li, born in 1978, is currently a professor and a PhD candidate supervisor at *Key Laboratory of E & M*, *Ministry of Education & Zhejiang Province*, *Zhejiang University of Technology*, *China*. He received his PhD degree from *Yanshan University*, *China*, in 2008. His research interests include parallel mechanism, robotics. E‐mail: lybrory@zjut.edu.cn

Zesheng Wang, born in 1994, is studying his PhD degree in *Zhejiang University of Technology*, *China*. His main research interests include parallel mechanism, hybrid mechanism, and robotics.

Chaoqun Chen, born in 1994, is studying his master degree in *Zhejiang University of Technology*, *China*. His main research interests include parallel mechanism, fluid transmission and control.

Taotao Xu, born in 1994, received his master degree from *Zhejiang University of Technology*, *China*. His main research interests include parallel mechanism, robotics.

Bo Chen, born in 1990, is currently a lecturer at Key Laboratory of E & M, Ministry of Education & Zhejiang Province, Zhejiang University of Technology, China. He received his PhD degree from Yanshan University, China, in 2018. His main research interests include parallel mechanism, fluid transmission and control. E‐mail: chenb@zjut.edu.cn

Competing interests

The authors declare no competing financial interests.

Acknowledgements

Funding

The authors gratefully acknowledge the support of the Zhejiang Provincial Natural Science Foundation for Distinguished Young Scientists [grant number LR18E050003]; the National Natural Science Foundation of China (NSFC) [grant number 51975523 and 51905481]; the China Postdoctoral Science Foundation [grant number 2020M671784]; and the Students in Zhejiang Province Science and technology Innovation Plan (Xinmiao Talents Program) [grant number 2020R403054].

References

[1] Y B Li, L Wang, B Chen, et al. Optimization of dynamic load distribution of a serial-parallel hybrid humanoid arm. *Mechanism and Machine Theory*, 2020, 149, 103792.

[2] P Sun, Y B Li, Z S Wang, et al. Inverse displacement analysis of a novel hybrid humanoid robotic arm. *Mechanism and Machine Theory*, 2020, 147, 103743.

[3] Y B Li, Z S Wang, P Sun, et al. Dynamic Load Distribution Optimization for a 4-DOF Redundant and Series-parallel Hybrid Humanoid Arm. *Journal of Mechanical Engineering*, 2020, 56(09):45-54. (in Chinese)

[4] Q C Li, L M Xu, Q H Chen, et al. New family of RPR-equivalent parallel mechanisms: design and application, *Chinese Journal of Mechanical Engineering*, 2017, 30 (2): 217-221.

[5] L J Zhang, X J Liu. On the design of the planar 2-DOF parallel manipulators with actuation redundancy. *Chinese Journal of Mechanical Engineering*, 2002, 38(12): 49-53.

[6] Z S Wang, Y B Li, Y Q Luo, et al. Dynamic analysis of a 7-DOF redundant and hybrid mechanical arm, *Journal of Mechanical Engineering*, 2020, 54(8): 1505-1515. (in Chinese)

[7] M J Thomas, M L Joy, A. P Sudheer. Kinematic and Dynamic Analysis of a 3-PR US Spatial Parallel Manipulator. *Chinese Journal of Mechanical Engineering*, 2020, 33(1), 1-17.

[8] B Chen, D R Gao, Y B Li, et al. Investigation of the droplet characteristics and size distribution during the collaborative atomization process of a twin-fluid nozzle. *International Journal of Advanced Manufacturing Technology*, 2020, 107(3-4): 1625–1639.

[9] G Chen, L Kong, Q Li, et al. Complete, minimal and continuous error models for the kinematic calibration of parallel manipulators based on POE formula. *Mechanism and Machine Theory*, 2018, 121: 844-856.

[10] C C Lurascu, F C Park. Geometric algorithms for kinematic calibration of robots containing closed loops. *Journal of Mechanical Design*, (2003)125(1), 23-32.

[11] M Abtahi, H Pendar, A Alasty, et al. Experimental kinematic calibration of parallel manipulators using a relative position error measurement system, *Robotics and Computer-Integrated Manufacturing*, 2010, 26(6): 799-804.

[12] X D Ren, Z R Feng, C P Su. A new calibration method for parallel kinematics machine tools using orientation constraint. *International Journal of Machine Tools and Manufacture*, 2009, 49(9): 708-721.

[13] B Chen, D R Gao, Y B Li, et al. Influence of atomizing core on droplet dynamic behavior and machining characteristics under synergistically enhanced twin-fluid spray. *International Journal of Advanced Manufacturing Technology*, https://doi.org/10.1007/s00170-020-05986-4.

[14] J I Jeong, D Kang, Y. M Cho, et al. Kinematic calibration for redundantly actuated parallel mechanisms. *Journal of Mechanical Design*, 2004, 126(2): 307-318.

[15] Y J Chiu, M. H. Perng. Self-calibration of a general hexapod manipulator using cylinder constraints. *International Journal of Machine Tools and Manufacture*, 2003, 43(10): 1051-1066.

[16] Y B Li, P Sun, H Qi, et al. Prototyping of a novel anthropomorphic mechanical leg. *Advances in Mechanical Engineering*, 2019, 11(12): 1-12.

[17] P Gao, K Li, L Wang, et al. A self-calibration method for accelerometer nonlinearity errors in triaxis rotational inertial navigation system. *IEEE transactions on Instrumentation and Measurement*, 2016, 66(2): 243-253.

[18] T Sun, Y Zhai, Y Song, et al. Kinematic calibration of a 3-DoF rotational parallel manipulator using laser tracker. *Robotics and Computer-Integrated Manufacturing*, 2016, 41: 78-91.

[19] D Zhang, Z Gao. Optimal kinematic calibration of parallel manipulators with pseudoerror theory and cooperative coevolutionary network. *IEEE Transactions on Industrial Electronics*, 2012, 59(8): 3221-3231.

[20] G Chen, X Rui, L K Abbas, et al. A novel method for the dynamic modeling of Stewart parallel mechanism. *Mechanism and Machine Theory*, 2018, 126: 397-412.

[21] S Staicu, D Zhang. A novel dynamic modelling approach for parallel mechanisms analysis. *Robotics and Computer-Integrated Manufacturing*, 2008, 24(1): 167-172.

[22] X Zhang, X Zhang, Z Chen. Dynamic analysis of a 3-RRR parallel mechanism with multiple clearance joints. *Mechanism and Machine Theory*, 2014, 78: 105-115.

[23] Y Yun, Y Li. Design and analysis of a novel 6-DOF redundant actuated parallel robot with compliant hinges for high precision positioning. *Nonlinear Dynamics*, 2010, 61(4): 829-845.

[24] G Bhutani, T A Dwarakanath. Novel design solution to high precision 3 axes translational parallel mechanism. *Mechanism and Machine Theory*, 2014, 75: 118-130.

[25] M Alberto, T Marco, C Marco, et al. Elastodynamic behavior of balanced close-loop mechanisms: Numerical analysis of a four-bar linkage. *Meccanica*, 2014, 49(3): 601-614.

[26] G Piras, W L Cleghorn, J K Mills. Dynamic finite-element analysis of a planar high-speed, high-precision parallel manipulator with flexible links. *Mechanism and Machine Theory*, 2005, 40: 849–862.

[27] H D Zhang, X M Zhang, X C Zhang, et al. Dynamic analysis of a 3-(P)under-barRR parallel mechanism by considering joint clearances. *Nonlinear Dynamics*, 2017, 90(1): 405-423.

[28] S Z Liu, J S Dai, A M Li, et al. Analysis of frequency characteristics

and sensitivity of compliant mechanisms. *Chinese Journal of Mechanical Engineering*, 2016, 29(04): 680-693.

[29] J Ryu, J Cha. Volumetric error analysis and architecture optimization for accuracy of HexaSlide type parallel manipulators. *Mechanism and Machine Theory*, 2003, 38(3): 227-240.

[30] Y B Li, H Zheng, P Sun, et al. Dynamic Modeling with Joint Friction and Research on the Inertia Coupling Property of a 5-PSS/UPU Parallel Manipulator. *Journal of Mechanical Engineering*, 2019, 55(03): 43-52. (in Chinese)

[31] Y B Li, H Zheng, B Chen, et al. Dynamic Modeling and Analysis of 5-PSS/UPU Parallel Mechanism with Elastically Active Branched Chains. *Chinese Journal of Mechanical Engineering*, 2020, 33(1): 1-12.

[32] S J Lee, B J Gilmore. The Determination of the Probabilistic Properties of Velocities and Accelerations in Kinematic Chains With Uncertainty. *Journal of Mechanical Design*, 1991, 113(1): 9-13.

[33] T Huang, D G Chetwynd, J P Mei, et al. Tolerance design of a 2-DOF overconstrained translational parallel robot. *IEEE Transactions on Robotics*, 2006, 22(1):167-172.

[34] D Liang, Y Song, T Sun. Nonlinear dynamic modeling and performance analysis of a redundantly actuated parallel manipulator with multiple actuation modes based on FMD theory. *Nonlinear dynamics*, 2017, 89(1): 391-428.

[35] R Cao, F Gao, Y Zhang, et al. A key point dimensional design method of a 6-DOF parallel manipulator for a given workspace. *Mechanism and Machine Theory*, 2015, 85: 1-13.

[36] W Dan, F Rui. Design and nonlinear analysis of a 6-DOF compliant parallel manipulator with spatial beam flexure hinges. Precision Engineering, 2016, 45: 365-373.

[37] Y Dong, F Gao, Y Yue. Modeling and experimental study of a novel 3-RPR parallel micro-manipulator. *Robotics and Computer-Integrated Manufacturing*, 2016, 37: 115-124.

Figures

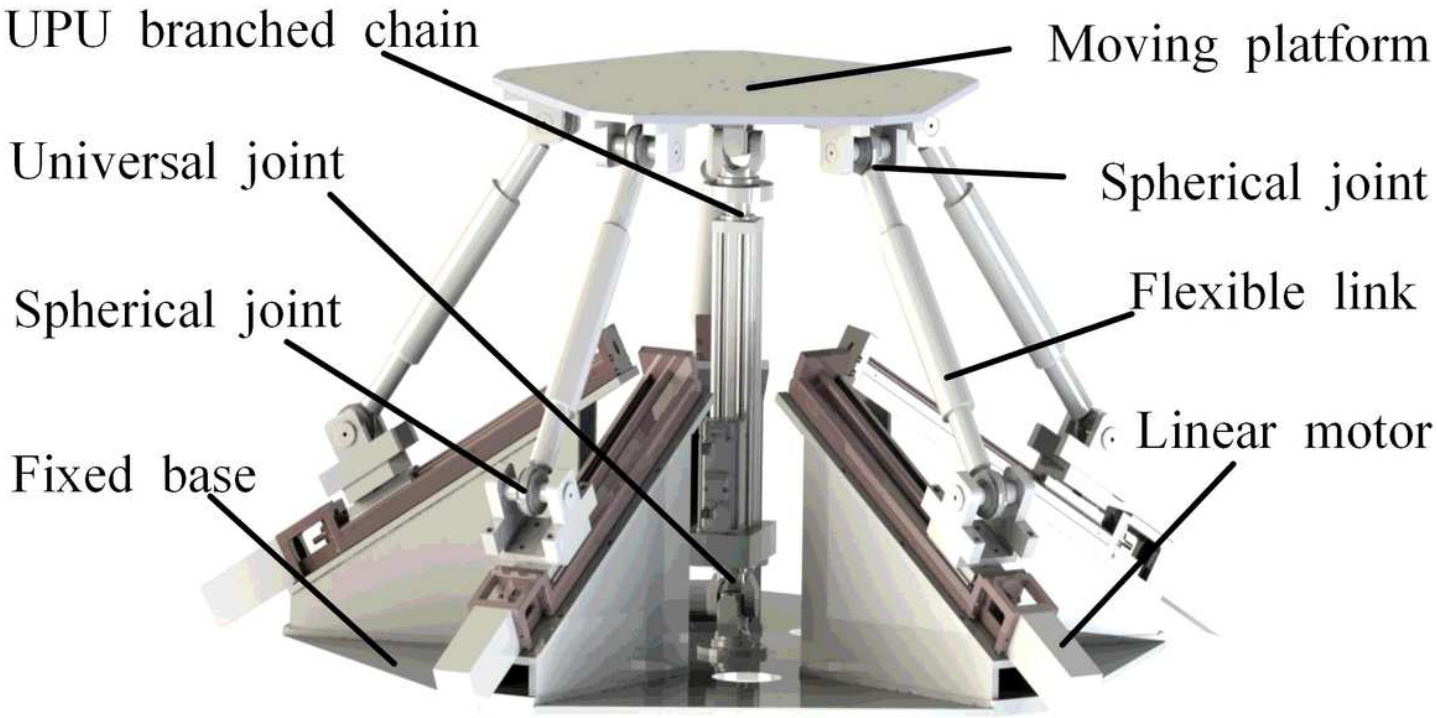

Figure 1

Virtual prototype of 5-PSS/UPU parallel mechanism

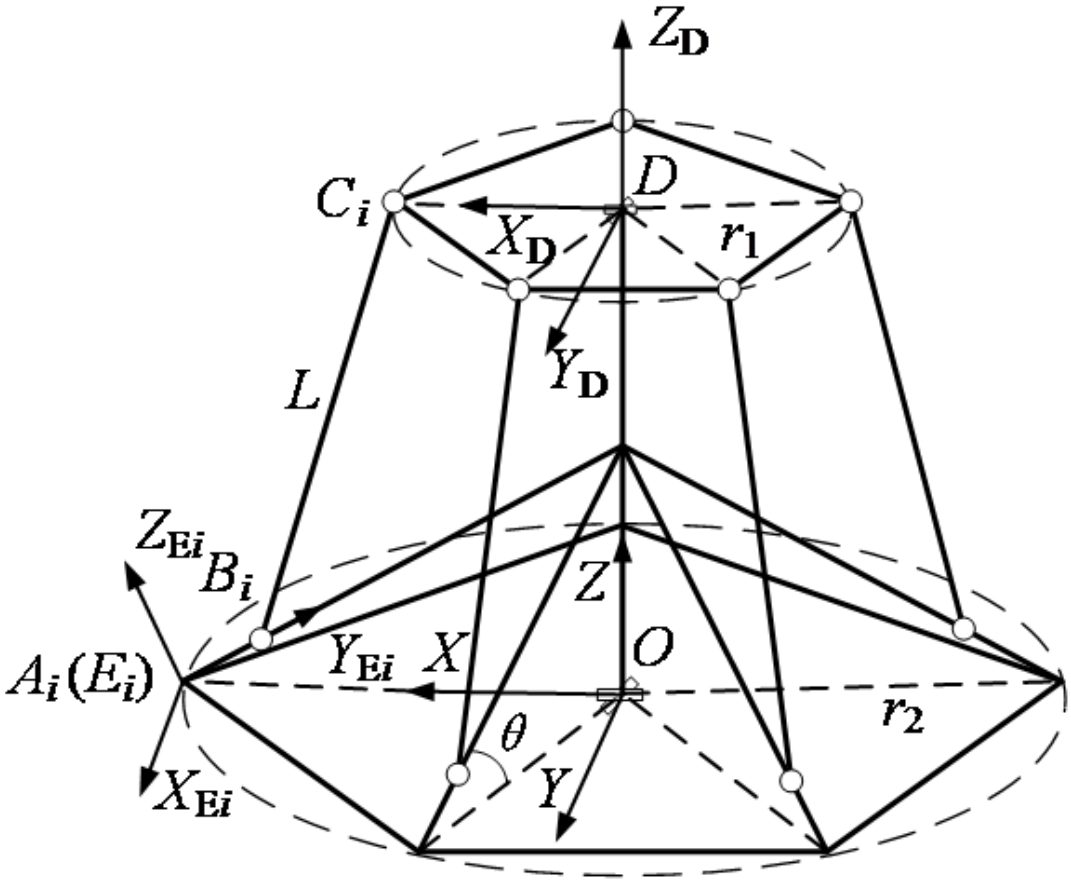

Figure 2

Structure diagram of 5-PSS/UPU parallel mechanism

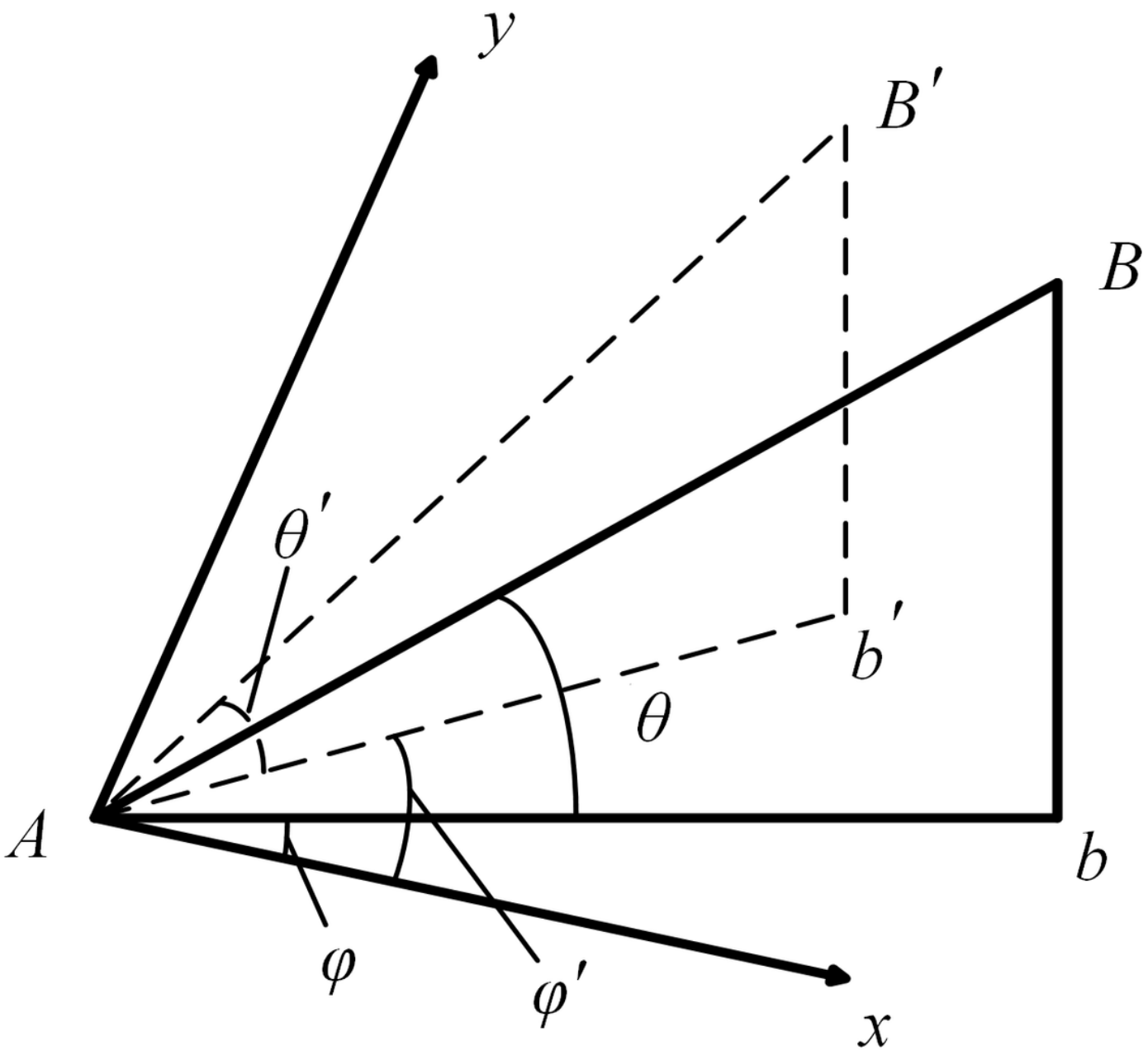

Figure 3

Linear motor direction vector error angle

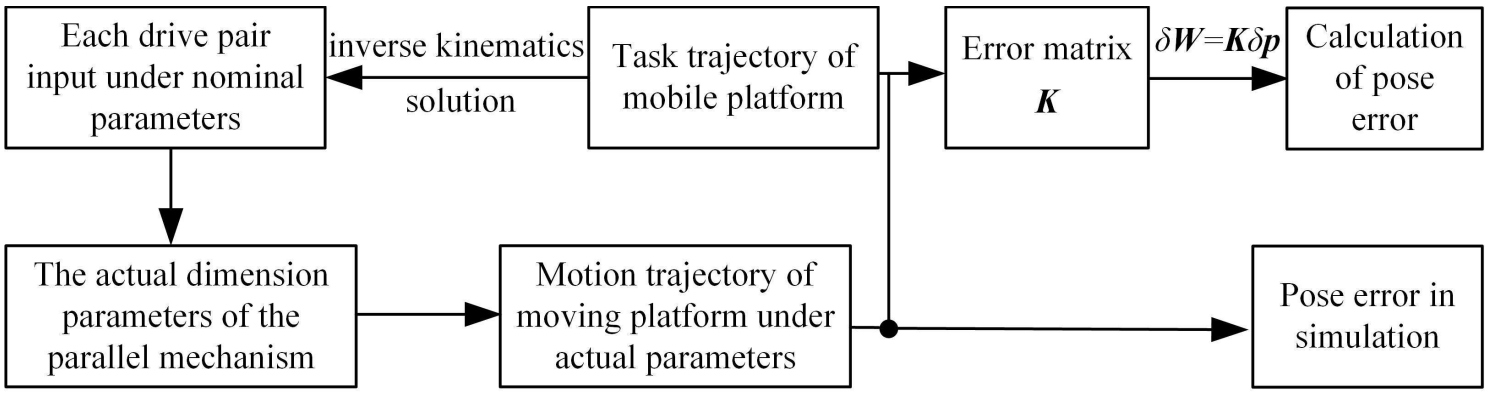

Figure 4

Analysis process of the influence of geometric errors on dynamic accuracy

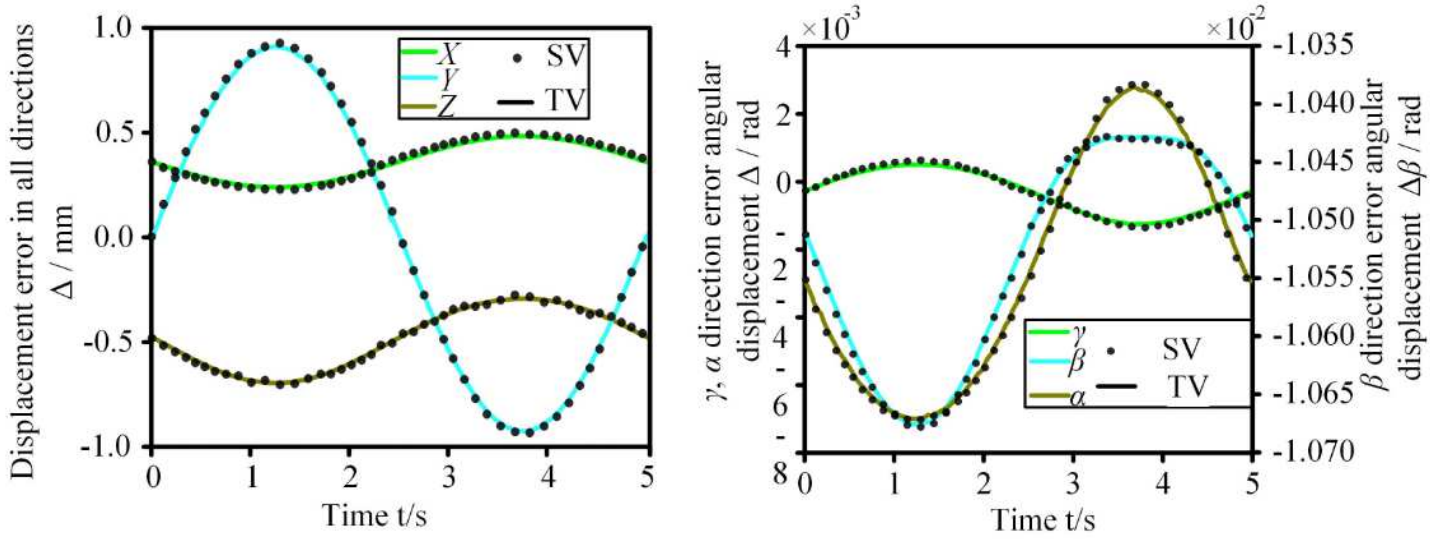

(a) Position displacement error of moving platform

(b) Pose displacement error of moving platform

Figure 5

Position and posture error sensitivity

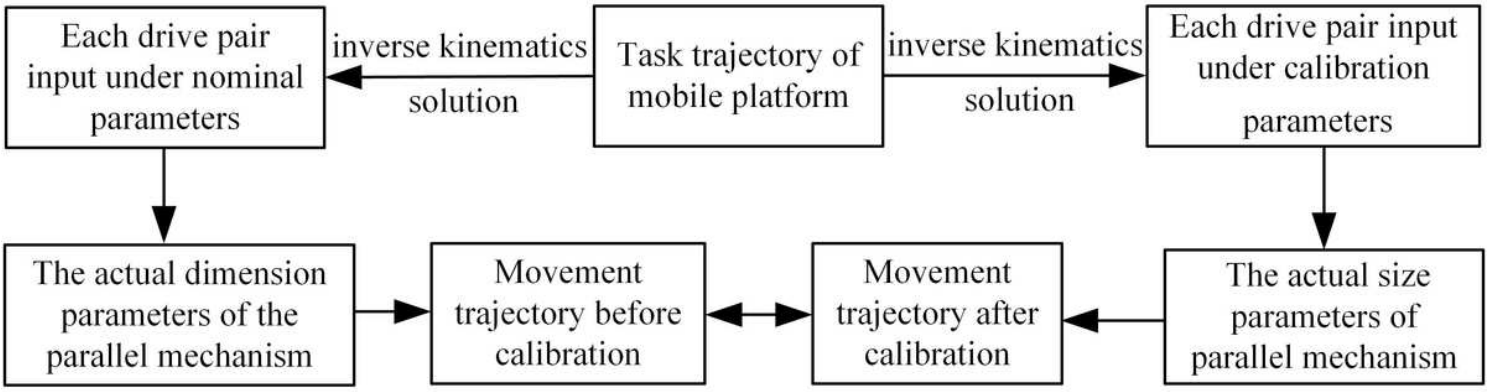

Figure 6

Comparison process of posture error before and after calibration

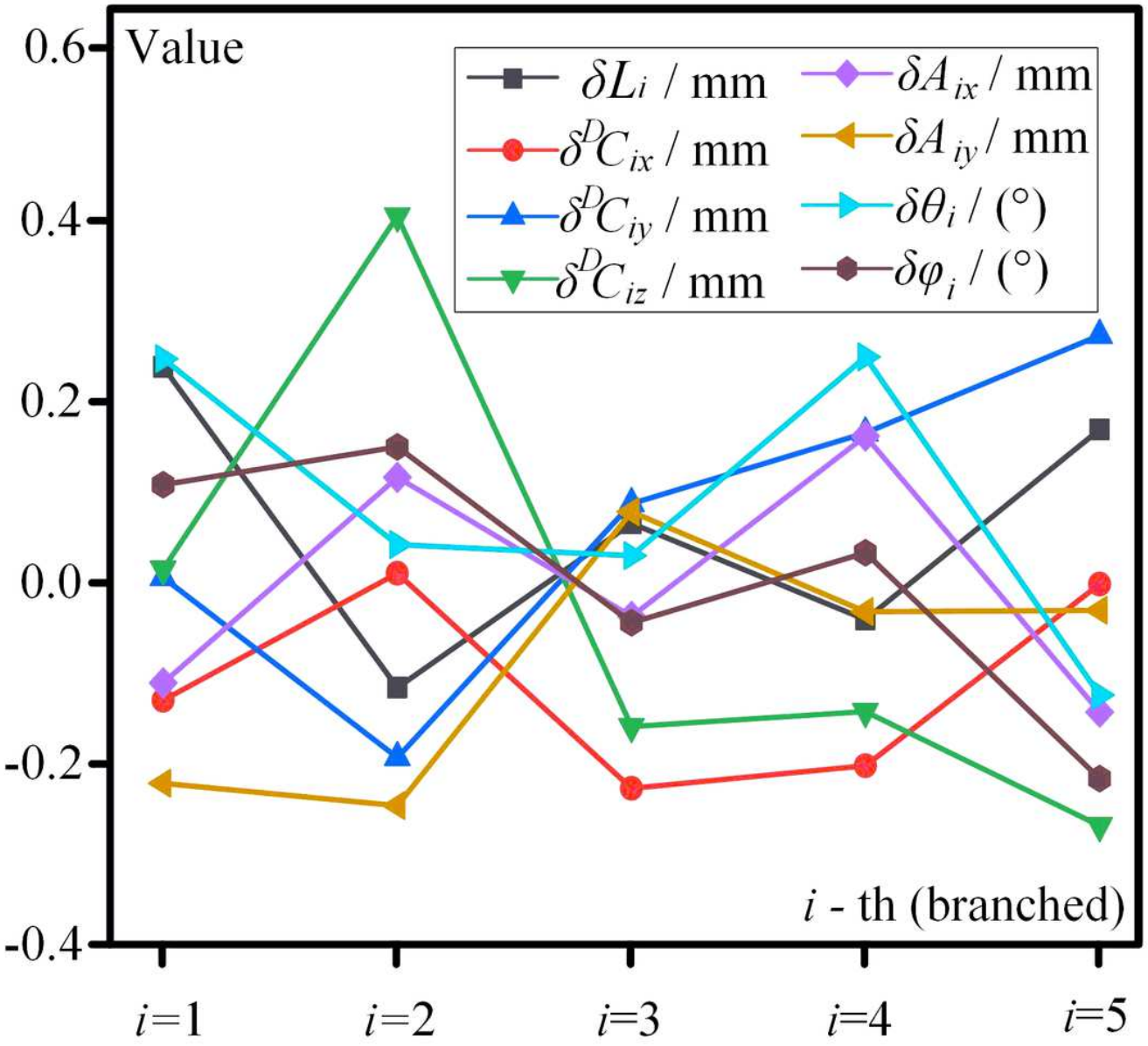

Figure 7

Error calibration values

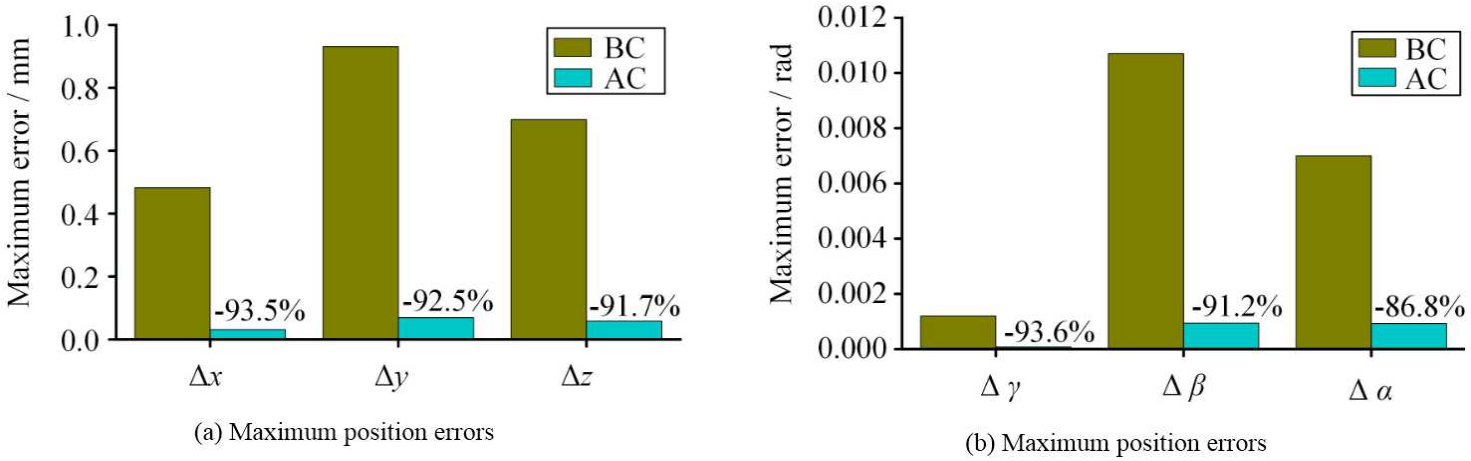

(a) Maximum position errors

(b) Maximum position errors

Figure 8

Comparison of posture errors before and after calibration

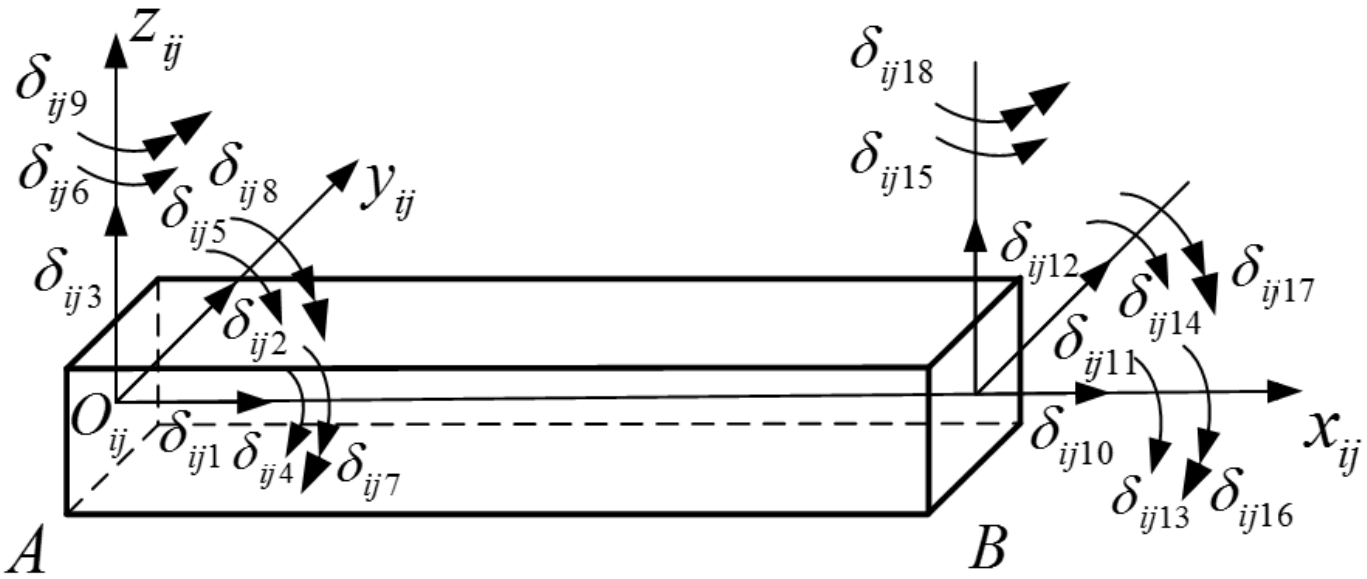

Figure 9

Spatial beam element model

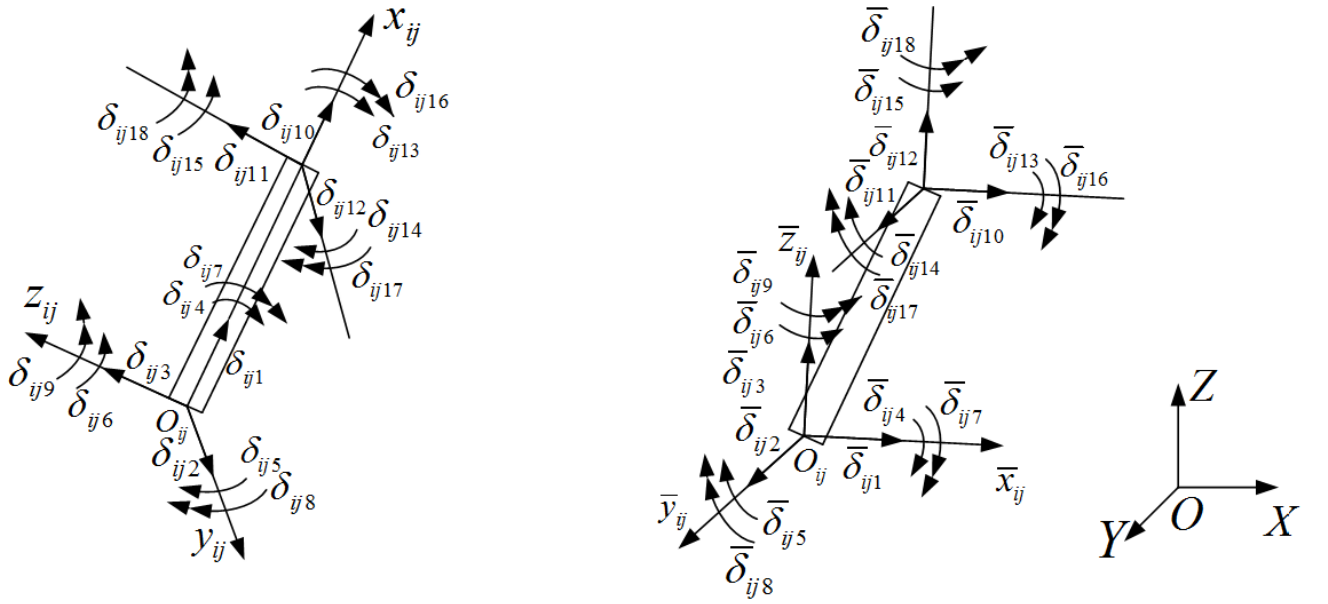

(a) Element generalized coordinates in link coordinate system

(b) Element generalized coordinates in base coordinate system

Figure 10

Unit coordinate system transformation

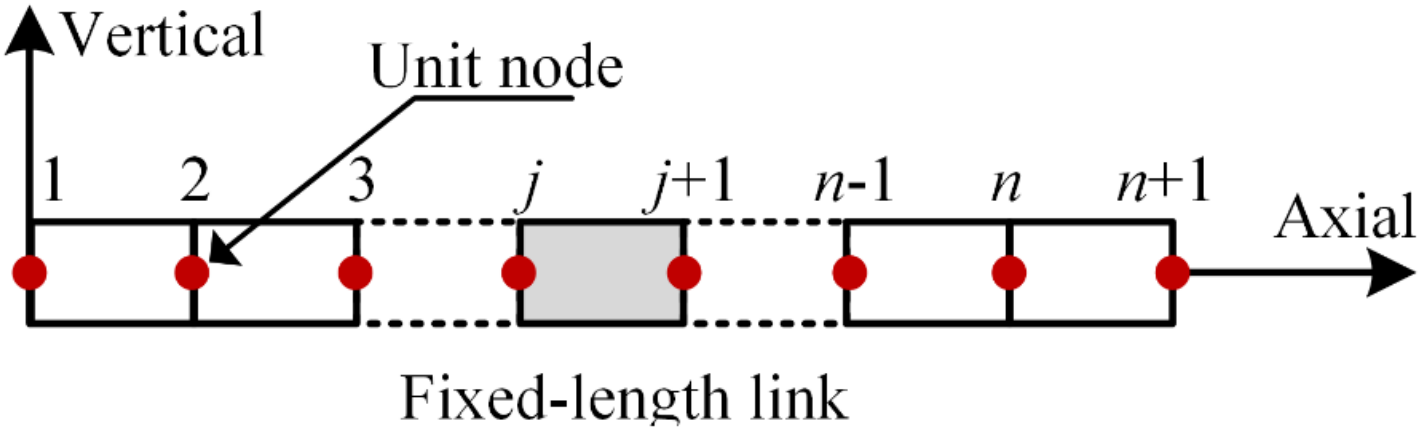

Figure 11

Division of the link unit

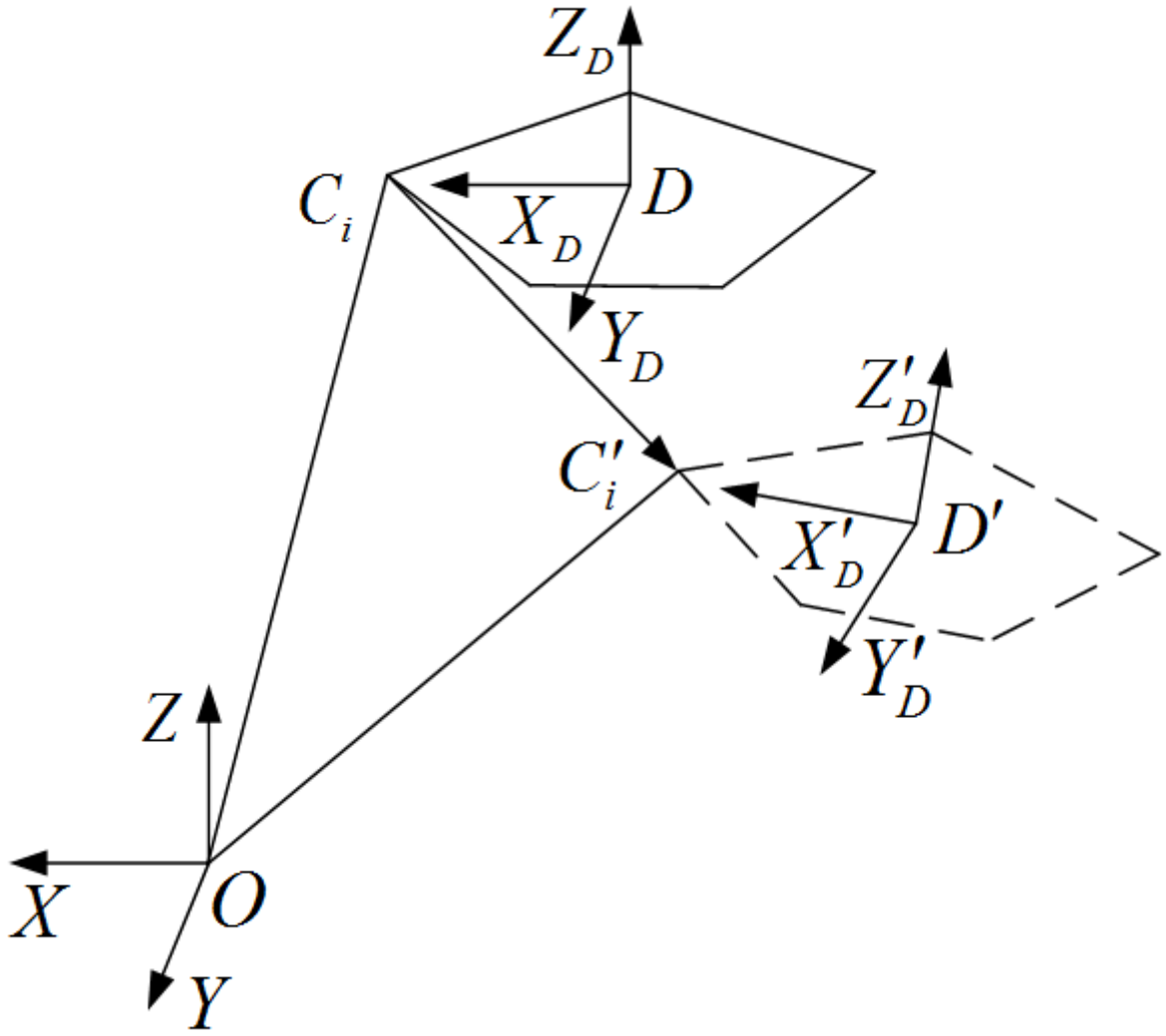

Figure 12

Constraints of system kinematics

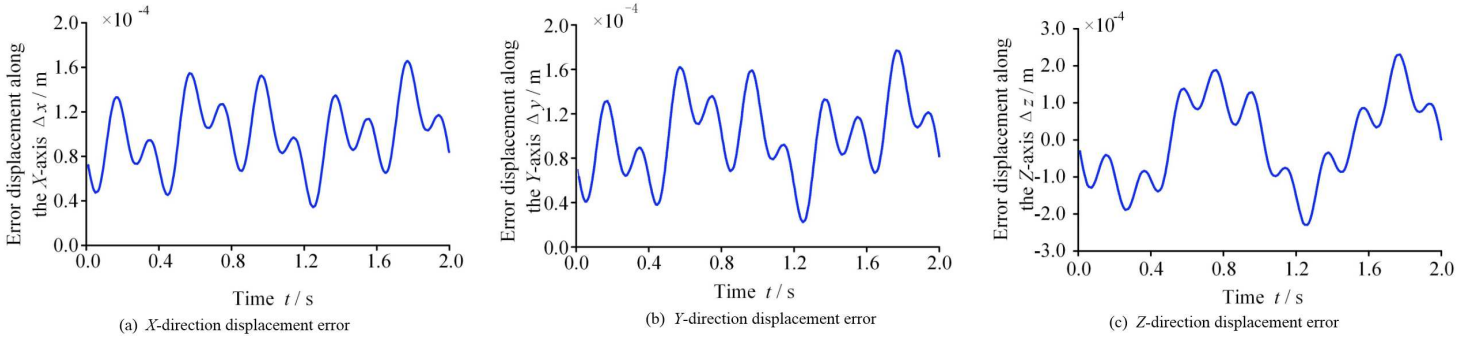

Figure 13

Position displacement error of moving platform

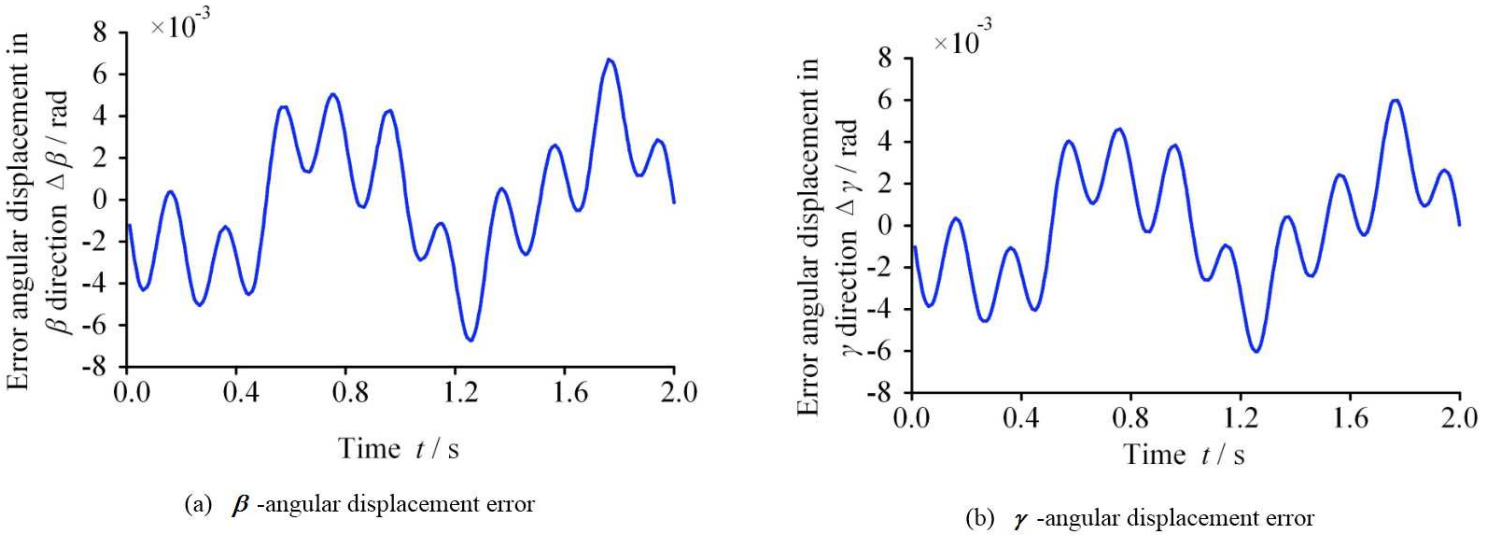

(a) β -angular displacement error

(b) γ -angular displacement error

Figure 14

Posture displacement error of moving platform

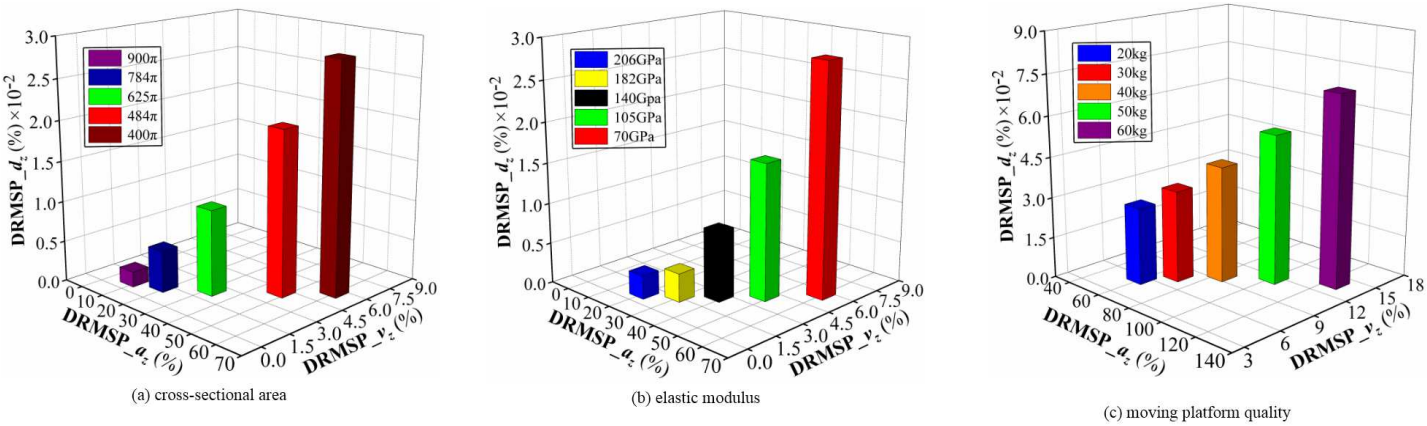

(a) cross-sectional area

(b) elastic modulus

(c) moving platform quality

Figure 15

Quantitative analysis of the output DRMSP(x)